Applied Energy 324 (2022) 119723

Contents lists available at ScienceDirect

Applied Energy

journal homepage: www.elsevier.com/locate/apenergy

Dual HESS electric vehicle powertrain design and fuzzy control based on multi-objective optimization to increase driving range and battery life cycle

Samuel Filgueira da Silva [a], Jony Javorski Eckert [a,*], Fernanda Cristina Corrêa [b], Fabrício Leonardo Silva [a], Ludmila C.A. Silva [a], Franco Giuseppe Dedini [a]

[a] Integrated Systems Laboratory, School of Mechanical Engineering - FEM University of Campinas - UNICAMP, Campinas, SP, Brazil
[b] Department of Electrical Engineering, Federal Technological University of Paraná, UTFPR Monteiro Lobato Avenue, Jardim Carvalho Ponta Grossa, PR, Brazil

GRAPHICAL ABSTRACT

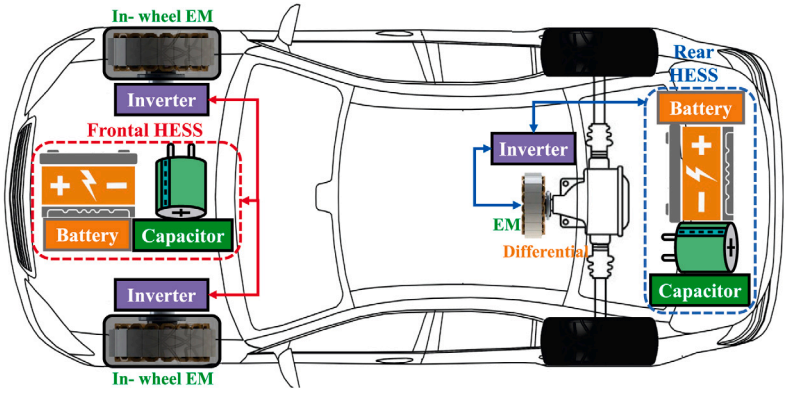

ARTICLE INFO

Keywords:
Electric vehicle
Hybrid energy storage system (HESS)
Fuzzy logic control
Battery state of health (*SoH*)
Multi-objective optimization

ABSTRACT

This study presents a comprehensive multi-objective optimization approach for a dual HESS-based electric vehicle (EV) powertrain using the interactive adaptive-weight genetic algorithm (i-AWGA) method. The dual HESS EV concept aims to show the benefits of combining independent traction systems powered by their respective energy sources. Therefore, the main purpose of this optimization is to simultaneously maximize driving autonomy and battery lifespan and minimize HESS size, considering design variables from components such as batteries, electric motors, differential, and ultracapacitors. At the same time, three independent fuzzy logic controllers – which perform the power management control between the hybrid energy storage systems – are likewise optimized, tuning their parameters according to the applied constraints. The best trade-off solution, equipped with a 332.34 kg dual HESS mass, achieved a driving range of 285.56 km and a front battery life cycle of 36585 h. As compared to a similar EV powered by a single HESS and optimized under the same driving conditions, the dual HESS EV improved the ratio between the driving range and energy storage system's overall mass by 3%, reaching a driving range 19.57% longer, and increasing the battery life by up to 22.88%.

* Corresponding author.
E-mail addresses: s263121@dac.unicamp.br (S.F. da Silva), javorski@fem.unicamp.br (J.J. Eckert), fernandacorrea@utfpr.edu.br (F.C. Corrêa), f208583@dac.unicamp.br (F.L. Silva), ludmila@fem.unicamp.br (L.C.A. Silva), dedini@fem.unicamp.br (F.G. Dedini).

https://doi.org/10.1016/j.apenergy.2022.119723
Received 31 March 2022; Received in revised form 2 July 2022; Accepted 17 July 2022
Available online 30 July 2022

1. Introduction

Over the last decades, regulatory policies focused on air quality management and energy security have extensively been implemented to tackle environmental, social, and economic issues related to high gas emission indexes and inefficient use of energy resources [1]. In this context, many countries have invested in clean and energy-saving technologies applied to the road transportation sector [2–4] as it contributes to 23% of the greenhouse gas emissions from fossil fuel combustion at the global scale [5] and consumes over 80 trillion megajoules of energy worldwide [6,7]. Further, the international sales of automobiles are forecast to double by 2050 [8], which emphasizes the need for the deployment of alternatively-powered vehicles to address climate change concerns.

Among the potential propulsion systems to substitute fossil fuel-based vehicles, the pure electric vehicles (EVs) are a promising alternative solution due to their carbon-neutral power source, low-noise operation, and high energy efficiency [9]. The energy storage systems (ESSs) play a crucial role in electric powertrain design since the development of extended-range EVs is still a challenging task to accomplish. At the same time, the advancement of automotive batteries during the last decade has enhanced EV reliability in terms of higher energy efficiency and longer operating time [10,11].

However, the commercially available battery technology's limitations stem from the difficulty of providing electrified vehicles with high specific power during driving conditions of peak load demands. Battery lifetime is reduced, due to substantial heat generation, by meeting high power requirements of electrically-propelled road vehicles [12]. In this sense, the hybrid energy storage systems (HESSs), consisting of an ultracapacitor and battery packs typically connected to a power converter, address this issue by supplying both averages, and peak power loads [13]. The combination of such distinct systems allows the EVs to operate during extended driving ranges using a high-energy-density battery while maintaining good vehicle performance due to the ultracapacitor that acts as a peak power buffer unit. Moreover, ultracapacitors (UCs) prevent regenerative braking energy harvesting from increasing battery degradation and perform energy regeneration at low-temperature conditions, in which conventional batteries could not correctly operate for this mode [14]. Hence, HESS configurations outperform battery-only ESSs concerning power density, battery lifespan, and energy savings [15].

In the literature, scholars have evaluated different HESS topologies for electric vehicles using an optimization process to maximize energy efficiency [16] and reduce operation cost [17]. In another approach, Wang et al. [18] proposed a HESS configuration that can operate in distinct modes such as hybrid output, regenerative braking, fully battery, and fully ultracapacitor modes. The multimode HESS enhanced overall system efficiency and reduced energy consumption for different driving cycles in their study.

Furthermore, energy management strategy (EMS), which can efficiently distribute power between the energy sources (batteries and UCs in this case), is of extreme importance for the HESS performance, efficiency, reliability, and durability [19–21]. Published works have implemented EMS for HESS based on several methods such as fuzzy logic control (FLC) approach [15,22], rule-based control (RBC) [23,24], model predictive control (MPC) strategy [14,25], filtration based control (FBC) strategy [26], learning-based strategy [27,28], wavelet-based strategy [29,30] etc. In the study of Song et al. [31], a comparative analysis of four distinct energy management control strategies (FLC, RBC, MPC, and FBC) for HESS of an all-electric bus showed that fuzzy-logic and rule-based controllers performed the best results, reducing over 50% of battery capacity loss when compared to the battery-only ESS configuration.

Optimization-based methods have also been extensively applied to power management for HESS in EVs. Researchers have formulated nonlinear optimization problems to investigate the optimal power split strategies for electrified vehicle powertrain equipped with HESS in order to increase driving range [32,33] and minimize system cost [34–36], energy consumption [26,37–39], battery degradation [38,40–42] and ultracapacitor losses [43]. Moreover, in order to optimize HESS components sizing, academics have used particle swarm optimization [44,45], Pontryagin's minimum principle [37], non-dominated sorting genetic algorithm type 2 (NSGA-II) [10], dynamic programming (DP) [35] among others. Zhang et al. [46] investigated the influence of HESS dimensioning on battery capacity fade using the NSGA-II approach to search for the best solutions concerning battery life, system weight, and cost. In the work of Yu et al. [15], HESS sizing and EV power split strategy based on fuzzy logic control are simultaneously optimized by an evolutionary algorithm. Such concurrent optimization of EMS and EV design parameters is also reported by the study of Li et al. [36], in which an adaptive random forests-based power-split control strategy is developed by obtaining the rules from the DP algorithm, and a HESS component sizing optimization is performed using multi-objective gray wolf optimizer.

Once the battery is still a bottleneck and significant component of EVs, scholars have studied the influence of battery lifespan on vehicle operating costs. To address this issue, battery life cycle model predictions have increasingly been carried out in the literature [47–50]. In the work of Hu et al. [51], a fractional-order model was developed to simultaneously estimate the battery state of charge and aging process under different driving conditions, achieving high accuracy compared to experimental results. In this way, aging-aware power management control strategies have proved crucial to preventing excessive battery stress and, reducing the life cycle costs of pure electric vehicles. Over the last years, aging-aware EMSs have been presented by several different studies [52–54]. In the study by Anselma et al. [55], a battery life sensitive off-line power-split control was implemented for a hybrid electric vehicle (HEV), resulting in a potential battery downsizing by 35% with no negative impact on the system lifespan. De Pascali et al. [56] designed a battery state-of-health conscious EMS for a parallel HEV powertrain architecture. The battery degradation could be reduced (up to 18%), while increasing fuel efficiency. In a different approach, Yuksel et al. [57] investigated the influence of driving profiles, thermal management strategies, and weather on the battery life cycle for a plug-in hybrid electric vehicle application. Additionally, researchers have used a battery charging capacity diagnostic framework to detect potential failures so that the safety of EV operation can be ensured [58].

Several works as [33,59] show the advantages of EVs, which combine EMs with different characteristics or assembly forms. Following this principle, EVs with a four-wheel-drive concept become a viable solution once the powertrain system is simplified [60,61]. These independent wheel traction EMs allow the power split control to determine the most efficient distribution according to the driving condition. The Independence Axiom proposed by Suh [62] indicates that components with multiple functional requirements should satisfy each one of these requirements without affecting the other ones. Therefore, EVs with independent traction systems should also present independent power sources once the discharges of each traction system directly interfere with the others in case a single power source is considered. This principle can be applied in the HESS system, which splits the current demand between the batteries' primary power source and ultracapacitors (high current peaks), improving the system efficiency. Still following the Independence Axiom principle, dividing the HESS among the available propelling systems can lead to optimized energy storage systems for their respective EM/drivetrain. Those independent HESS can be smaller and more efficient once they do not need to be robust to fulfill the current peaks of all EV motors compared to EVs powered by a single HESS.

In previous work, Eckert et al. [32] present the concept of a dual HESS electric vehicle, which applies to the same principle of the independence of the traction system for the energy storage. The proposed EV presented two independent HESSs, one for the frontal in-wheel

EMs and another that powers the EM/differential system applied to the rear wheels. The mentioned propelling system configuration was also successfully applied in previous works [33,61], which showed the advantages of this EV powertrain architecture that combines different EMs characteristics, allowing such system to reach high efficiency in different driving conditions such as urban, highway traffic or even at high power demand conditions. The dual HESS-based EV concept, also studied in this paper, is presented in Fig. 1.

The proposed dual HESS electric vehicle increased the driving range to 145.15 km with a HESS 23.93% lighter than the results presented in [63] for a similar EV powered by a single HESS. Despite these gains, none of those previous EV optimization works considers the maximization of the battery lifespan as an optimization criterion. Battery degradation is an essential factor to be considered, since pure electric powertrain architectures cause more battery stress than hybrid electric ones [64]. Once the battery is one of the critical EV powertrain components and responsible for a significant parcel of the total cost of ownership [20,65,66], the use of battery-ultracapacitor HESS in EVs will only be economically advantageous if the implemented EMS results in extended battery life cycle expectation [39]. In addition, premature replacement of batteries, which is directly associated with high depth of discharge and current fluctuations [67–70], causes adverse environmental effects. This is because the automotive batteries-making process depends upon polluting manufacturing plants [71], while battery disposal is still a major concern as reported by different studies in the literature [72–74]. Recharging time can also be considered a drawback for plug-in electric vehicles concerning sustainable aspects. First, large-scale electric vehicle charging demand may become a significant issue for cities lacking robust electricity supply infrastructure [75–78]. Second, the long EV charging process is associated with higher operational costs [79–82]. Lastly, the need for great electric power generation to supply public and residential EV recharging stations makes EVs responsible for greenhouse gas emissions in case such electricity comes from polluting energy sources [83,84].

Based on the presented state of the art, there are no studies about optimizing a dual HESS EV regarding the benefits of this configuration in the battery lifespan and EV operational costs compared to the traditional single HESS EV. In this context, the novelty of this work remains from the fact that multi-objective optimization design of dual HESS-based EV powertrain considering energy efficiency simultaneously, driving range, recharging time, and battery aging effects has not been comprehensively carried out in the literature to date. Given this fact, the current work aims to fulfill this research gap, showing the advantages of using this proposed EV powertrain topology rather than the conventional single HESS-equipped one.

Therefore, this study presents a multi-objective optimization of a dual HESS EV, in which the drivetrain (EMs and differential), HESS sizing (battery and ultracapacitors), and the fuzzy controllers responsible for the traction power distribution between the EMs and also the discharge split between battery and ultracapacitors for both HESSs are optimized. This EV configuration is optimized to maximize the EV driving range, minimize the overall dual HESS mass and, improve the battery's state of health based on an estimated life cycle. In order to provide a fair comparison, the same EV powered only by a single HESS is also optimized, considering the same applied criteria. Finally, both optimization problems are solved by employing the interactive adaptive-weight genetic algorithm (i-AWGA) to find the best trade-off among the optimization criteria.

The optimization will be conducted under the FTP-75, HWFET and US06 driving cycles, which are the same applied in previous works [32,63], intending to provide an EV configuration that is robust to different driving scenarios. This robustness of the optimized dual HESS EVs is also evaluated under the WLTC standard cycle and four real-world driving cycles, which correspond to driving conditions different from the ones in which the EVs were optimized. In this context, the changes of battery lifetime caused by different driving conditions are also analyzed. Moreover, a comparative costs analysis is carried out between the dual-HESS optimum solutions and other EVs architectures. Finally, the main contribution of this study are:

- Dual HESS EV architecture aiming improvement in the EV drive range and batteries' life cycle
- Multi-objective optimization procedure of the overall EV powertrain and fuzzy logic control, aiming to improve driving range, energy storage mass, and battery life cycle
- Comparison with a similar EV powered by a single HESS, optimized under the same conditions applied to the dual HESS EV
- Powertrain cost benchmark among the optimized dual and single HESS EVs configurations
- Evaluation of the optimum dual HESS EV under four real-world driving cycles

2. Simulation model

The vehicle simulation model is based on the longitudinal dynamics presented by Gillespie [85] and adapted to the EV drivetrain configuration in a previous work [32]. The first step is to define the EV power demand, represented by the required traction torque T_{req} [Nm] at the vehicle wheels. As expressed by Eq. (1), such variable T_{req} is calculated as a function of the movement resistance forces such as the

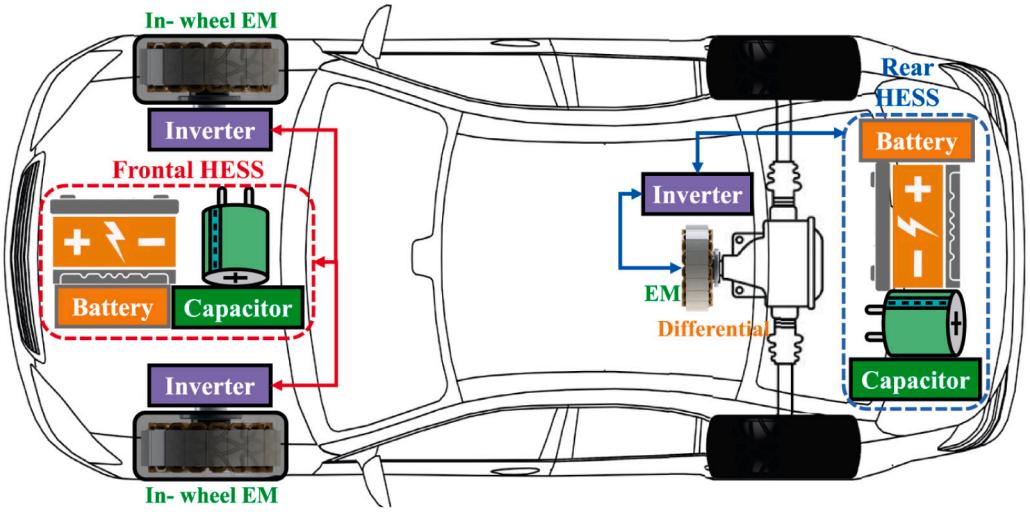

Fig. 1. Dual HESS EV concept.

aerodynamic drag D_A [N] (Eq. (2)) and tires rolling resistance R_x [N] (Eq. (3)).

$$T_{req} = \left(R_x + D_A + M a_{req}\right) r \tag{1}$$

$$D_A = \frac{1}{2}\rho V^2 C_D\ A \tag{2}$$

$$R_x = 0.01\left(1 + \frac{2.24\ V}{100}\right) M g \tag{3}$$

where M [kg] and V [m/s] represent the vehicle mass and speed respectively, g [m/s^2] is the gravitational acceleration, r [m] is the tire's radius, ρ [kg/m^3] corresponds to the air density, and the vehicle shape is represented by the frontal area A [m^2] and the drag coefficient C_D.

The required acceleration a_{req} [m/s^2] is defined by comparing the current vehicle speed $V(t)$ with the driving cycle target speed V_c at time step Δ_t [s] ahead of the current simulation time t [s] as shown in Eq. (4) [86].

$$a_{req}(t) = \frac{V_c(t + \Delta_t) - V(t)}{\Delta_t} \tag{4}$$

As mentioned before, in this paper, the simulation will be based on three driving cycles with different speed profiles: FTP-75 (urban driving), HWFET (highway driving), and the US06 (high speed and required acceleration). The selected driving cycle speed profiles are presented in Fig. 2.

Considered the EV required torque to reach the cycle target speed, the fuzzy power split control, which will be discussed in details in Section 3, outputs the $0 \leq P_S \leq 1$ value that distributes the traction torque demand between the frontal T_{reqF} [Nm] and rear T_{reqR} [Nm] propelling systems as presented in Eqs. (5) and (6).

$$T_{reqF} = P_S T_{req} \tag{5}$$

$$T_{reqR} = (1 - P_S) T_{req} \tag{6}$$

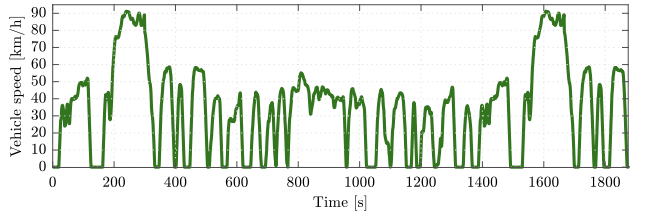

(a) FTP-75

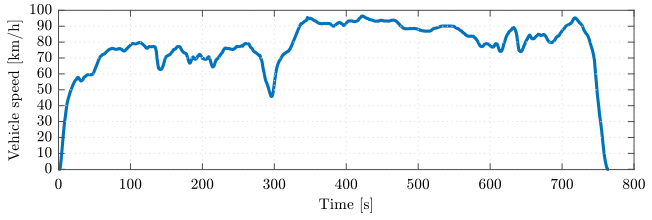

(b) HWFET

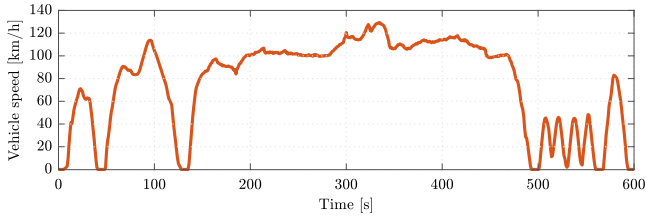

(c) US06

Fig. 2. Simulated driving cycles [87,88].

Each torque demand is then converted to correspond to the load applied to the respective EMs of each drive system. For the frontal system, the T_{reqF} values are divided between two in-wheel EMs according to Eq. (7) considering the inertia of the frontal wheels and EMs assembled into them I_{wf} [kgm^2].

$$T_{EMF} = \frac{T_{reqF} + I_{wf}\frac{a_{req}}{r}}{2} \tag{7}$$

In the case of the rear system, a single EM is coupled to a differential transmission, with gear ratio N_d, mechanical efficiency η_d and inertia I_d [kgm^2], which is added to the rear wheels' inertia I_{wr} [kgm^2] as expressed by Eq. (8).

$$T_{EMR} = \frac{T_{reqR} + \left(I_d N_d^2 + I_{wr}\right)\frac{a_{req}}{r}}{N_d \eta_d} \tag{8}$$

The required torque value for each EM (T_{EMF} and T_{EMR}) are then compared to the available torque through their respective torque curves (see Fig. 3a). If the available maximum torque $T_{A(F,R)}$ [Nm] is lower than the requested value, the vehicle acceleration will be limited. Another key parameter to be analyzed regarding traction of the EMs is the transmissible torque in the tire-ground contact, which can significantly decrease the vehicle acceleration performance [89,90]. The maximum transmissible torque is defined by Eqs. (9) and (10) proposed by Jazar [91] as a function of the tire-ground friction peak coefficient μ, vehicle gravity center height h [m] and wheelbase L [m] and the longitudinal distances between the gravity center and the rear c [m] and frontal b [m] axles, respectively. For the initial condition, the vehicle acceleration a_x [m/s^2] is considered equal to the required acceleration ($a_x = a_{req}$).

$$T_{F(max)} = \mu\left(\frac{M g\ c}{2L} - \frac{M h\ a_x}{2L}\right) r \tag{9}$$

$$T_{R(max)} = \mu\left(\frac{M g\ b}{2L} + \frac{M h\ a_x}{2L}\right) r \tag{10}$$

The traction torques that are effectively applied by the frontal T_F [Nm] and rear T_R [Nm] propelling systems are defined by Eqs. (11) and (12).

$$T_F = \min\begin{cases} 2T_{EMF} - I_{wf}\frac{a_x}{r} \\ 2T_{AF} - I_{wf}\frac{a_x}{r} \\ T_{F(max)} \end{cases} \tag{11}$$

$$T_R = \min\begin{cases} T_{EMR} N_d \eta_d - \left(I_d N_d^2 + I_{wr}\right)\frac{a_x}{r} \\ T_{AR} N_d \eta_d - \left(I_d N_d^2 + I_{wr}\right)\frac{a_x}{r} \\ T_{R(max)} \end{cases} \tag{12}$$

Finally, the EV acceleration is determined by Eq. (13). However, several values regarding the calculation of T_F and T_R torques are directly dependent on a_x parameter. Therefore, an iterative process among Eqs. (9) to (13) is performed until convergence.

$$a_x = \frac{T_F + T_R - \left(D_A + R_x\right) r}{M r} \tag{13}$$

After convergence, the effective torque values for the frontal T_{Fef} [Nm] and rear T_{Ref} [Nm] are calculated by Eqs. (14) and (15).

$$T_{Fef} = \frac{T_F + I_{wf}\frac{a_x}{r}}{2} \tag{14}$$

$$T_{Ref} = \frac{T_R + \left(I_d N_d^2 + I_{wr}\right)\frac{a_x}{r}}{N_d \eta_d} \tag{15}$$

Table 1 presents the EV parameters applied in the simulations.

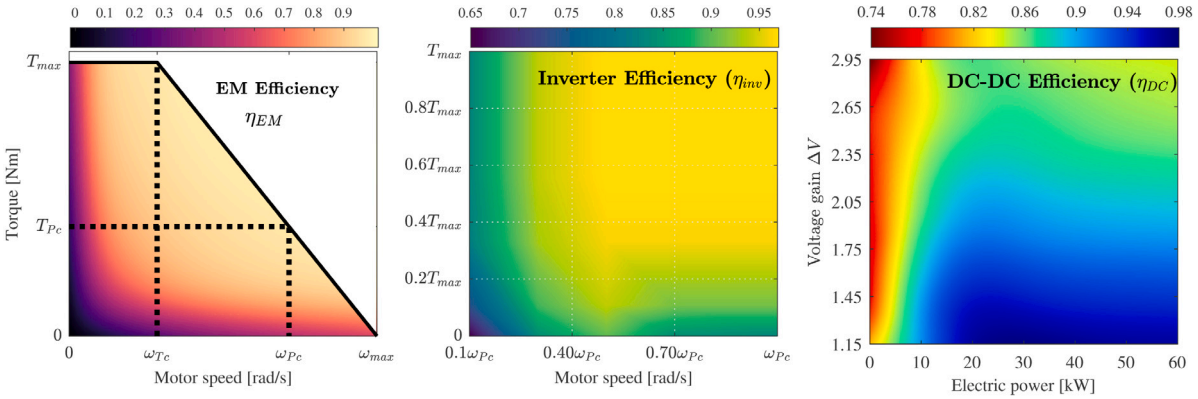

(a) EM efficiency [61, 92] (b) inverter efficiency [61, 93] (c) DC-DC converter efficiency

Fig. 3. Electric motors, inverter and DC–DC converter efficiency maps.

Table 1
Vehicle parameters [32,61].

Vehicle mass without HESS	800 kg
Tires 175/70 R13 radius (r)	0.2876 m
Wheels + tires inertia (I_w)	2 kgm^2
Tire peak friction coefficient (μ)	0.9
Vehicle frontal area (A)	1.8 m^2
Drag coefficient (C_D)	0.33
Differential efficiency (η_{id})	0.9
Wheelbase (L)	2.443 m
Gravity center height (h)	0.53 m
Front axle to gravity center (b)	0.983 m
Rear axle to gravity center (c)	1.460 m

2.1. Electric motors model

The design of the front in-wheel and rear EMs is an essential factor for potential improvements in EV performance and energy efficiency. In this manuscript, a generic EM torque curve is presented, being defined according to reference operating points of motor speed ω_{Tc} [rad/s] at constant (maximum) torque phase as well as constant-power-phase torque T_{Pc} [Nm] (which represents 30% of maximum motor torque T_{max} [Nm], as expressed by Eq. (16)) and speed ω_{Pc} [rad/s] (Eq. (17)). This method was developed in previous work [61], based on available EM data and literature information [92], complemented by experiments performed in an instrumented flywheel bench presented in the work of Yamashita et al. [93].

$$T_{Pc} = 0.3T_{max} \tag{16}$$

$$\omega_{Pc} = \frac{T_{max}\omega_{Tc}}{T_{Pc}} \tag{17}$$

In addition, the maximum motor speed ω_{max} [rad/s] (when EM torque is null) is defined by linear progression based on the aforementioned torque curve points, that is, (T_{max}, ω_{Tc}) and (T_{Pc}, ω_{Pc}). In this sense, the i-AWGA method optimizes these design variables that define EMs' torque curves, as previously presented by published studies [32,94,95]. The inverter efficiency map is based on the work of Rotering et al. [96], adapted to be used in optimization [61]. The generic efficiency maps of the electric motors and inverters are depicted in Fig. 3ab. Based on the operating region, it is possible to determine the EMs' efficiencies for front η_{EMF} and rear η_{EMR} propulsion systems. The inverters' ($\eta_{EM(F/R)}$) and DC bus ($\eta_{DC(F/R)}$) efficiencies are defined analogously. Hence, the electrical current profile delivered to frontal I_F [A] and rear I_R [A] can then be calculated by Eqs. (18) and (19), respectively, as a function of the current HESS voltage for each drive system $V_{H(F/R)}$ [V].

$$I_F = \frac{2T_{Ref}V}{r\,V_{HF}\,\eta_{EMF}\,\eta_{invF}\,\eta_{DCF}} \tag{18}$$

$$I_R = \frac{T_{Ref}VN_d}{r\,V_{HR}\,\eta_{EMR}\,\eta_{invR}\,\eta_{DCR}} \tag{19}$$

The EMs can operate as generators during braking conditions, performing energy regeneration to recharge the ultracapacitors. In this study, the motors can harvest braking energy until 10% of their available torque capacities. Additionally, a low vehicle speed threshold of 15 km/h is established for the EM ability to operate in regenerative braking energy mode since low-speed condition causes limited electromotive force generation [97,98].

2.2. Battery-ultracapacitor HESS model

A DC–DC converter is employed to connect the ultracapacitor and battery pack power sources to the drive system [99]. Power converters used for a HESS require bidirectional power flow, securing high-efficiency charging, and discharging of the system [100]. For that reason, the HESS applied in this study was assembled using the parallel DC–DC converters topology (Fig. 4).

This topology presents high precision power demand distribution to the sources. Also, it offers high stability and flexibility in its operations, with a smooth current flow (a better solution for voltage variation), but has control complexity and increased semiconductor switches [101].

Utilizing a system with parallel converters, it is possible to enter a negative power flow exclusively in the ultracapacitor, which is characterized as having high charge and discharge capacity. Hence, it is necessary for a buck-boost converter in an ultracapacitor to act as a boost when discharging and as a buck when undercharging [102]. The battery converter is a boost, simply taking part in the discharge process [103].

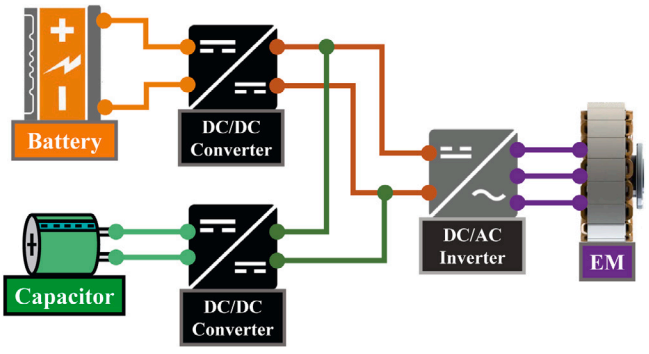

Fig. 4. HESS topology.

Fig. 3c presents the DC–DC converter efficiency map (that is based on the data presented in the literature [104]), in which the voltage gain ΔV (y-axis) represents the ratio between the output voltage delivered by the DC–DC converter and the input voltage supplied by the energy storage system. By Fig. 3c, it is possible to observe that the DC–DC converter efficiency η_{DC} has a significant influence on such voltage amplification and the electric power supplied by the system. A higher voltage gain for the same provided electric power results in lower DC–DC converter efficiency.

2.2.1. Ultracapacitor model

In this study, a generic ultracapacitor model is implemented according to the database of 16 ultracapacitor configurations $Cap(n)$ available in the market, as described in Table 2. The optimization procedure (Section 4) is responsible for defining the UCs arrangement, which can be associated in series or parallel configuration or even combined in a pack with UCs in series and parallel at the same time. The evolutionary algorithm also tuned the number of ultracapacitors in series N_s per branch and the number of branches in parallel N_p. The overall mass of the associated ultracapacitors M_{cap} [kg] (Eq. (20)) can then be calculated as a function of the mass $M_{uc(n)}$ [kg] of the selected ultracapacitor $Cap(n)$.

$$M_{cap(F/R)} = N_{s(F/R)}\ N_{p(F/R)}\ M_{uc(n_{F/R})} \tag{20}$$

Furthermore, the equivalent voltage V_{Ceq} [V], capacitance C_{eq} [F] and resistance R_{Ceq} [Ω] of the association of ultracapacitors can be defined by Eqs. (21)–(23), respectively.

$$V_{Ceq} = \sum_{i=1}^{N_s} V_{Ci} \tag{21}$$

$$C_{eq} = \sum_{k=1}^{N_p} \left(\frac{1}{\sum_{i=1}^{N_s} \frac{1}{C_i}} \right)_k \tag{22}$$

$$R_{Ceq} = \left(\sum_{k=1}^{N_p} \left(\frac{1}{\sum_{i=1}^{N_s} R_i} \right)_k \right)^{-1} \tag{23}$$

The ultracapacitor state of charge SoC_C [%], on the other hand, is determined according to the initial electric charge Q_{ini} [C], the electrical current I_{cap} [A], and the actual electric charge Q_T [C], as expressed by Eq. (24).

$$SoC_C(t) = \left(\frac{Q_{ini} - \int_0^t I_{cap}(\tau) d\tau}{Q_T} \right) \times 100 \tag{24}$$

Table 2
Ultracapacitor parameters [32].

$Cap(n)$	$V_{uc(n)}$ [V]	$C_{uc(n)}$ [F]	$R_{uc(n)}$ [Ω]	$M_{uc(n)}$ [kg]
$Cap(1)$	16	108	3.6E−03	3.0
$Cap(2)$		108	4.3E−03	3.7
$Cap(3)$		200	3.5E−03	4.1
$Cap(4)$		266	3.0E−03	4.6
$Cap(5)$		333	2.4E−03	5.1
$Cap(6)$		500	1.9E−03	6.0
$Cap(7)$	48	36	13E−03	9.5
$Cap(8)$		66	10.4E−03	11.5
$Cap(9)$		88	8.9E−03	12.5
$Cap(10)$		111	7.1E−03	13.5
$Cap(11)$		166	5.6E−03	16.0
$Cap(12)$	64	83	9.5E−03	17.0
$Cap(13)$		125	7.5E−03	20.0
$Cap(14)$	86	62	12.7E−03	21.0
$Cap(15)$		93	10E−03	26.0
$Cap(16)$	125	62	15E−03	67.0

2.2.2. Battery model

The battery state of charge SoC_B [%] is considered a key parameter in the investigation of the energy storage system behavior under different operational conditions [105] since it indicates the available battery capacity. In the simulation, the defined electrical current $I_{batt(F/R)}$ is delivered to the lithium-ion battery model, which is based on Simulink™ battery block database. SoC_B can then be estimated by Eq. (25), as a function of the current profile I [A], initial state of charge $SoC_B(t_0)$ [%] and battery capacity Q [Ah]. Since the actual state of charge is defined, the depth of discharge DoD [%] can also be calculated, as expressed by Eq. (26).

$$SoC_B(t) = SoC_B(t_0) - \left(\frac{1}{Q(3600)} \int_0^t I_{batt}(\tau) d\tau \right) \times 100 \tag{25}$$

$$DoD(t) = 100 - SoC_B(t) \tag{26}$$

As described in Section 3, the state of charge is introduced as one of the input parameters of the fuzzy logic energy management control. It is also worth pointing out that the SoC_B range is limited to 40% to avoid excessive discharge, which results in the shortening of the battery life cycle. Regarding the battery mass M_{bat} [kg] for front and rear drive systems, this parameter is given by Eq. (27), as a function of the typical lithium-ion battery specific energy (S_E = 150 [Wh/kg] [106,107]), nominal voltage V_{nom} [V] and nominal capacity Q_{nom} [Ah].

$$M_{bat(F/R)} = \frac{V_{nom(F/R)} Q_{nom(F/R)}}{S_E} \tag{27}$$

Furthermore, the battery voltage dynamics is defined according to the Shepherd model [108–110]. The actual voltage V_{batt} [V] is determined by Eqs. (28) and (29) for the charge and discharge modes, respectively. The calculation of V_{batt} is given as function of the battery current I_{batt} [A], constant voltage of battery equivalent circuit E_0 [V], polarization constant K [V(Ah)$^{-1}$], battery internal resistance R [Ω], exponential zone time constant inverse B [(Ah)$^{-1}$], exponential zone amplitude A [V] and filtered current I^* [A], which can assume negative (charging) or positive (discharging) values.

$$V_{batt}^{(I^*<0)} = E_0 - RI_{batt} - K\left(\frac{Q}{I_{batt}t - 0.1Q} \right) I^* - K\left(\frac{Q}{Q - I_{batt}t} \right) I_{batt}t + Ae^{-BI_{batt}t} \tag{28}$$

$$V_{batt}^{(I^*>0)} = E_0 - RI_{batt} - K\left(\frac{Q}{Q - I_{batt}t} \right) I^* - K\left(\frac{Q}{Q - I_{batt}t} \right) I_{batt}t + Ae^{-BI_{batt}t} \tag{29}$$

After the vehicle model has been subjected to the combined driving cycle (Fig. 2), the battery recharging process is simulated, considering the final SoC_B (at the end of travel) as the initial charging condition. In the literature, the non-linearity of battery charging behavior has comprehensively been investigated by researchers [111,112]. In this paper, charging electrical current I_c [A] is defined as constant to reduce the computational cost of the multi-objective optimization model. The constant I_c value is determined according to the maximum voltage V_c [V]. The battery can reach [94,113] so that such allowable voltage should be not exceeded until the complete charge condition (SoC_B = 100%). In this sense, the required energy to recharge the battery J_c [Ws] is calculated by Eq. (30), where C_t [s] and η_c are the recharging time and efficiency factor associated with heat and AC–DC conversion power losses, respectively.

$$J_c = \int_0^{C_t} \eta_c I_c V_c dt \tag{30}$$

As mentioned previously, the battery capacity fade is introduced as a design parameter in the multi-objective optimization, so earlier substitution of this key EV powertrain component can be prevented. The implemented aging model is a generic approach used for different types

of lithium-ion batteries, as proposed by Motapon et al. [114]. It does not require costly and time-consuming procedures to obtain a large amount of data for each analyzed battery configuration, thereby consisting of a suitable approach for optimization methods due to decrease of computational burden. Additionally, such capacity fade model has been reported to be accurate when compared to experimental results. In this study, the battery degradation model sets a standard value for the ambient temperature (T_{amb} = 293.15 K), disregarding temperature effects on individual battery cells. Moreover, since the ultracapacitor lifetime is much greater than that of the EV itself, its aging can be neglected [52,115].

The actual capacity Q [Ah] for the presented lithium-ion battery aging model can be expressed by Eq. (31), where Q_{BOL} and Q_{EOL} correspond to the battery capacity at the beginning-of-life (BOL) and end-of-life (EOL) conditions, respectively. The aging factor ϵ varies along the nth half cycle, in which a full cycle is characterized by the combined process of discharging and recharging. In addition, the maximum number of cycle Cl is determined as a function of the cycle number constant H, nominal ambient temperature T_{ref} [K], Arrhenius rate constant ψ, average current for the half-cycle in charge I_c [A] and discharge I_d [A] modes, and exponent factors for depth of discharge ξ, discharge current γ_d and charge current γ_c.

$$Q(n) = Q_{BOL} - \epsilon(n)(Q_{BOL} - Q_{EOL}) \tag{31}$$

$$\epsilon(n) = \epsilon(n-1) + \frac{1}{2Cl(n-1)}\left(2 - \frac{DoD(n-2) + DoD(n)}{DoD(n-1)}\right) \tag{32}$$

$$Cl(n) = H\left(\frac{DoD(n)}{100}\right)^{-\xi} \times exp\left(-\psi\left(\frac{1}{T_{ref}} - \frac{1}{T_{amb}(n)}\right)\right)(I_d^a(n))^{-\gamma_d}(I_c^a(n))^{-\gamma_c} \tag{33}$$

The battery state of health SoH depicts the current working condition of the system when compared to the lithium-ion battery capacity at the beginning of life, that is, $SoH = 1$. In this sense, the SoH value, which its decrease is directly associated with battery durability issues [116], can be estimated by Eq. (34) [117]. Furthermore, the ISO standard 12 405 [118] defines that the battery should reach its EOL capacity (Q_{EOL}) when the actual capacity is reduced to 80% of the capacity at the beginning of life (Q_{EOL}), that is, $\epsilon = 0$. Finally, to further evaluate the battery life cycle for each configuration obtained by the optimization method, the simulation model is subjected to a 3000-h cycling test.

$$SoH(n) = \frac{Q(n)}{Q_{BOL}} \tag{34}$$

3. Fuzzy logic control

Fuzzy inference control systems have extensively been used for several engineering applications such as power management control of hybrid electric [119], plug-in hybrid electric [94,120,121], fuel cell electric [122] and pure electric vehicles [22,32], as well as gear shifting control [90,95,123], vehicle handling [124–126], photovoltaic systems [127,128], wind energy conversion systems [129], hybrid renewable energy systems [130], thermal control systems [131,132] etc. Hence, the fuzzy logic approach, which is reported to present robustness and anti-disturbance capacity, is adopted in this work for the development of an optimal energy management control strategy that aims to efficiently split requested power between the front and rear propulsion systems as further described in the following Section 3.1. Moreover, as the second stage of power management control (PMC), independent fuzzy-logic controllers are likewise introduced to distribute energy between the ultracapacitor and battery of each HESS (Section 3.2).

It is also important to highlight that the formulation of fuzzy logic controller's parameters (membership functions, rules, and weights) is often defined based on acquired experience from experts, which makes the optimization of fuzzy logic control a complex task to achieve [133]. Hence, this work addresses this issue by tuning the design parameters of fuzzy logic energy management and HESS power split controllers using the i-AWGA method. The optimization procedure could prevent the fuzzy logic controllers from any biased formulation.

Finally, since Mamdani fuzzy control has successfully been applied to electrified vehicle powertrain architectures [32,63,134], this inference method is used for the proposed controllers, which are established according to the Matlab™ fuzzy logic toolbox.

3.1. Energy management control

The fuzzy-logic power management control features linear membership functions since they guarantee advantages of lower computational cost and less complexity, thereby extensively being used as an effective alternative in the literature [95,135]. The trapezoidal function type is selected as it presents a broader range of combinations to form the membership function of any level when compared to triangular ones.

For such energy distribution between front and rear propulsion systems, the fuzzy control is composed of three inputs, which are defined by the overall efficiency of the rear η_R and front η_F system, as well as the required torque T_{req}. The fuzzy output, on the other hand, is given by the parameter P_S, which corresponds to a unitary-range value

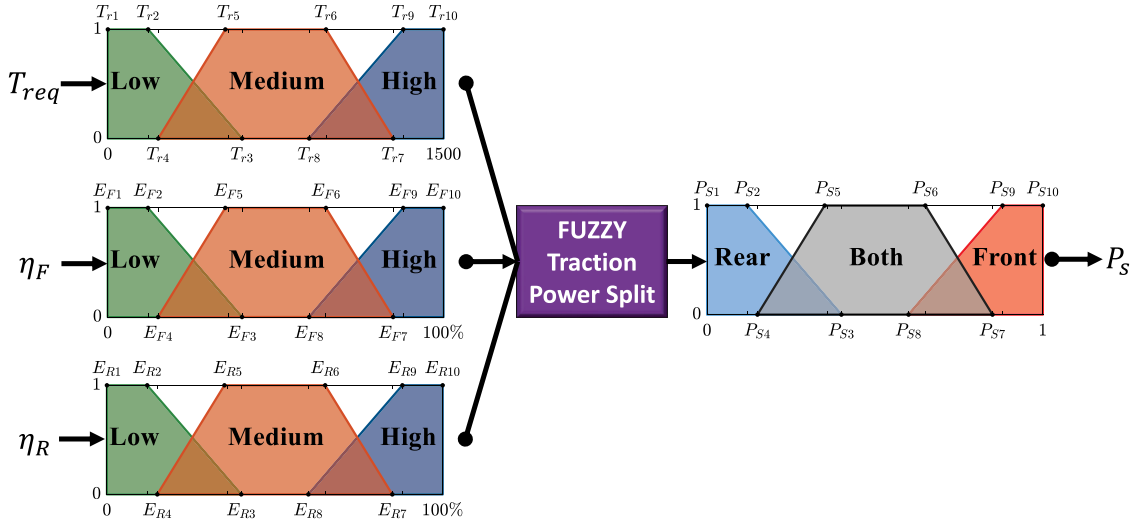

Fig. 5. Electric motors power split control.

that determines the suitable parcel of torque delivered to each electric drive system (see Eqs. (5) and (6)). Concerning the degrees, the fuzzy membership functions are divided into three generic categories: low L_d, medium M_d, and high H_d, in which 10 points characterize each group of input/output membership functions, as depicted by Fig. 5.

Hence, the vector $\mathbf{MF_{PS}}$ that represents all membership functions can be defined by Eq. (35), where $[T_{ri}\ E_{Fi}\ E_{Ri}]$ and P_{Si} are associated to the fuzzy inputs and output, respectively. Moreover, the input's combination of the three fuzzy degrees is performed using the "AND" connection, resulting in 27 possible output rules R_{pi} and their respective weights W_{pi} (Table 3), which vary in the interval from 0 through 1. Eq. (36) presents the vector $\mathbf{RW_{PS}}$ that comprises the fuzzy controller's rules and weights. The defuzzification method D_{z1}, (energy distribution between the rear and front), on the other hand, was set as the centroid to prevent abrupt changes in the fuzzy output value, which would be hard to accomplish in realistic driving conditions [95].

$$\begin{aligned}\left[\mathbf{MF_{PS}}\right]_{1\times32} = \big[&T_{r2}\ T_{r3}\ldots T_{r8}\ T_{r9}\ E_{F2}\ E_{F3}\ldots\\ &E_{F8}\ E_{F9}\ E_{R2}\ E_{R3}\ldots E_{R8}\ E_{R9}\ P_{S2}\ P_{S3}\ldots P_{S8}\ P_{S9}\big]\end{aligned} \tag{35}$$

$$\left[\mathbf{RW_{PS}}\right]_{1\times54} = \left[R_{p1}\ R_{p2}\ \ldots\ R_{p27}\ W_{p1}\ W_{p2}\ldots W_{p27}\right] \tag{36}$$

It should also be underlined that the fuzzy logic control must satisfy the constraints C_{fuzzy} (Eq. (37)), which indicates the limitations regarding possible combinations of membership functions' characteristic points F_{Mi} as well as output rules R_{jk} (an integer number from 1 to 3, representing low, medium and high degrees, respectively) and weights W_{jk}.

$$C_{fuzzy} = \begin{cases} F_{M1} < F_{M2} < F_{M3} \\ F_{M4} < F_{M5} < F_{M6} < F_{M7} \\ F_{M8} < F_{M9} < F_{M10} \\ F_{M1} < F_{M3} < F_{M8} < F_{M10} \\ F_{M1} < F_{M4} < F_{M3} \\ F_{M8} < F_{M7} < F_{M10} \\ F_{M2} < F_{M5} < F_{M6} < F_{M9} \\ 1 \le R_{jk} \le 3 \\ 0 \le W_{jk} \le 1 \end{cases} \tag{37}$$

3.2. Battery-ultracapacitor HESS control

Analogously to the power distribution control between the front and rear propulsion systems, the battery-ultracapacitor HESS power split is performed by a fuzzy-logic controller, featuring trapezoidal input/output membership functions, as illustrated by Fig. 6. Three inputs characterize this fuzzy control: the front/rear requested power $P_{F/R}$, the front/rear battery state of charge $SoC_{B(F/R)}$ and the front/rear ultracapacitor state of charge $SoC_{C(F/R)}$. In this sense, the vector $\mathbf{MF_{HS(F/R)}}$ (Eq. (38) for the front system and Eq. (39) for the rear one) corresponds to the input/output membership functions' parameters, in which $[P_{ri}\ S_{Bi}\ S_{Ci}]$ and H_{Si} represent the inputs and output, respectively. Regarding the fuzzy rules R_{hi} and weights W_{hi}, the vectors $\mathbf{RW_{HS(F)}}$ and $\mathbf{RW_{HS(R)}}$ (Table 4) store these design variables of the HESS controllers from the front and rear propulsion systems, respectively, as expressed by Eqs. (40) and (41). Additionally, the defuzzification methods (D_{z2} and D_{z3}) for the HESS fuzzy logic controllers are added to the $\mathbf{RW_{HS(F/R)}}$ vectors as parameters to be tuned by the genetic algorithm. The D_{z2} and D_{z3} can assume value of 1 (centroid), 2 (bisector), 3 (middle of maximum), 4 (largest of maximum) or 5 (smallest of maximum). Besides, the HESS fuzzy controllers are likewise subjected to the constraints mentioned earlier shown in Eq. (37).

$$\begin{aligned}\left[\mathbf{MF_{HS(F)}}\right]_{1\times32} = \big[&P_{r2}\ P_{r3}\ldots P_{r8}\ P_{r9}\ S_{B2}\ S_{B3}\ldots\\ &S_{B8}\ S_{B9}\ldots S_{C2}\ S_{C3}\ldots S_{C8}\ S_{C9}\ H_{S2}\ H_{S3}\ldots H_{S8}\ H_{S9}\big]\end{aligned} \tag{38}$$

$$\begin{aligned}\left[\mathbf{MF_{HS(R)}}\right]_{1\times32} = \big[&P_{r12}\ P_{r13}\ldots P_{r18}\ P_{r19}\ S_{B12}\ S_{B13}\ldots\\ &S_{B18}\ S_{B19}\ S_{C12}\ S_{C13}\ldots S_{C18}\ S_{C19}\ H_{S12}\ H_{S13}\ldots H_{S18}\ H_{S19}\big]\end{aligned} \tag{39}$$

$$\left[\mathbf{RW_{HS(F)}}\right]_{1\times55} = \left[R_{h1}\ R_{h2}\ \ldots\ R_{h27}\ W_{h1}\ W_{h2}\ldots W_{h26}\ W_{h27}\ D_{z2}\right] \tag{40}$$

$$\begin{aligned}\left[\mathbf{RW_{HS(R)}}\right]_{1\times55} = \big[&R_{h28}\ R_{h29}\ \ldots\ R_{h54}\ W_{h28}\ W_{h29}\ldots\\ &W_{h53}\ W_{h54}\ D_{z3}\big]\end{aligned} \tag{41}$$

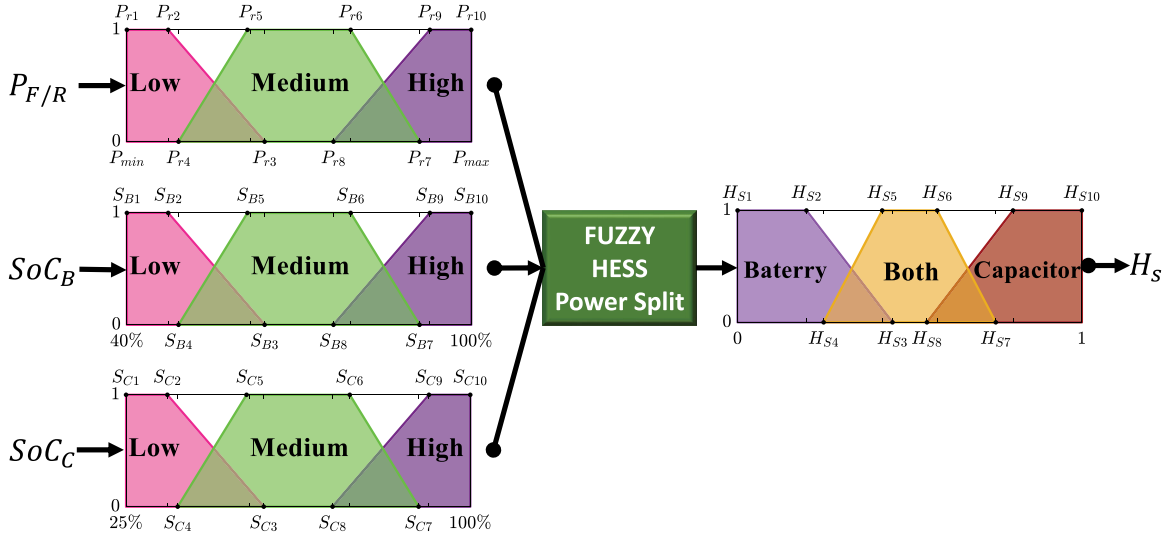

Fig. 6. HESS power split controls.

Table 3
Power distribution control rules.

		Traction torque split		
η_R	η_F	T_{req}		
		L_d	M_d	H_d
L_d	L_d	$R_{p1}\ W_{p1}$	$R_{p2}\ W_{p2}$	$R_{p3}\ W_{p3}$
	M_d	$R_{p4}\ W_{p4}$	$R_{p5}\ W_{p5}$	$R_{p6}\ W_{p6}$
	H_d	$R_{p7}\ W_{p7}$	$R_{p8}\ W_{p8}$	$R_{p9}\ W_{p9}$
M_d	L_d	$R_{p10}\ W_{p10}$	$R_{p11}\ W_{p11}$	$R_{p12}\ W_{p12}$
	M_d	$R_{p13}\ W_{p13}$	$R_{p14}\ W_{p14}$	$R_{p15}\ W_{p15}$
	H_d	$R_{p16}\ W_{p16}$	$R_{p17}\ W_{p17}$	$R_{p18}\ W_{p18}$
H_d	L_d	$R_{p19}\ W_{p19}$	$R_{p20}\ W_{p20}$	$R_{p21}\ W_{p21}$
	M_d	$R_{p22}\ W_{p22}$	$R_{p23}\ W_{p23}$	$R_{p24}\ W_{p24}$
	H_d	$R_{p25}\ W_{p25}$	$R_{p26}\ W_{p26}$	$R_{p27}\ W_{p27}$

Table 4
HESS control rules.

Front HESS control					Rear HESS control				
$SoC_{B(F)}$	$SoC_{C(F)}$	P_F			$SoC_{B(R)}$	$SoC_{C(R)}$	P_R		
		L_d	M_d	H_d			L_d	M_d	H_d
L_d	L_d	R_{h1} W_{h1}	R_{h2} W_{h2}	R_{h3} W_{h3}	L_d	L_d	R_{h28} W_{h28}	R_{h29} W_{h29}	R_{h30} W_{h30}
	M_d	R_{h4} W_{h4}	R_{h5} W_{h5}	R_{h6} W_{h6}		M_d	R_{h31} W_{h31}	R_{h32} W_{h32}	R_{h33} W_{h33}
	H_d	R_{h7} W_{h7}	R_{h8} W_{h8}	R_{h9} W_{h9}		H_d	R_{h34} W_{h34}	R_{h35} W_{h35}	R_{h36} W_{h36}
M_d	L_d	R_{h10} W_{h10}	R_{h11} W_{h11}	R_{h12} W_{h12}	M_d	L_d	R_{h37} W_{h37}	R_{h38} W_{h38}	R_{h39} W_{h39}
	M_d	R_{h13} W_{h13}	R_{h14} W_{h14}	R_{h15} W_{h15}		M_d	R_{h40} W_{h40}	R_{h41} W_{h41}	R_{h42} W_{h42}
	H_d	R_{h16} W_{h16}	R_{h17} W_{h17}	R_{h18} W_{h18}		H_d	R_{h43} W_{h43}	R_{h44} W_{h44}	R_{h45} W_{h45}
H_d	L_d	R_{h19} W_{h19}	R_{h20} W_{h20}	R_{h21} W_{h21}	H_d	L_d	R_{h46} W_{h46}	R_{h47} W_{h47}	R_{h48} W_{h48}
	M_d	R_{h22} W_{h22}	R_{h23} W_{h23}	R_{h24} W_{h24}		M_d	R_{h49} W_{h49}	R_{h50} W_{h50}	R_{h51} W_{h51}
	H_d	R_{h25} W_{h25}	R_{h26} W_{h26}	R_{h27} W_{h27}		H_d	R_{h52} W_{h52}	R_{h53} W_{h53}	R_{h54} W_{h54}

Additionally, the output value H_S determines the fraction of requested power performed by the battery and ultracapacitor. Thus, the battery power P_{batt} [W] and ultracapacitor power P_{cap} [W] are defined by Eqs. (42) and (43), respectively, where S_{reg} represents the decision-making process that determines whether the ultracapacitor is able to operate in discharging mode or not. Such state variable S_{reg} (Eq. (44)) was introduced to avoid ultracapacitor over-discharge (after the system has reached any SoC_C value lower than 25%) or to prevent discharge in case of the system after discharging until the low SoC_C limit of 25%, has not regenerated enough energy yet to reach a minimum state of charge SoC_{reg}, which varies from 35% to 95% according to the optimization method (Section 4).

$$P_{batt} = \begin{cases} P_{F/R} H_S, & \text{if } S_{reg} = 0 \text{ and } P_{F/R} > 0 \\ P_{F/R}, & \text{if } S_{reg} = 1 \text{ and } P_{F/R} > 0 \\ 0, & \text{if } P_{F/R} \leq 0 \end{cases} \tag{42}$$

$$P_{cap} = \begin{cases} P_{F/R}(1 - H_{S(F/R)}), & \text{if } S_{reg} = 0 \text{ and } P_{F/R} > 0 \\ 0, & \text{if } S_{reg} = 1 \text{ and } P_{F/R} > 0 \\ P_{F/R}, & \text{if } P_{F/R} \leq 0 \end{cases} \tag{43}$$

$$S_{reg}(t) = \begin{cases} 1, & \text{if } \begin{cases} SoC_C(t) < 25\%, \text{ or:} \\ S_{reg}(t - \Delta t) = 1 \text{ and } SoC_C(t) < SoC_{reg} \end{cases} \\ 0, & \text{if } \begin{cases} SoC_C(t) \geq SoC_{reg}, \text{ or:} \\ S_{reg}(t - \Delta t) = 0 \text{ and } SoC_C(t) \geq 25\% \end{cases} \end{cases} \tag{44}$$

4. Optimization procedure

This section introduces the multi-objective optimization problem's formulation, highlighting each of the optimization criteria considered in this study. Moreover, the evolutionary algorithm procedure is described and applied to reach optimal powertrain design variables and fuzzy logic controller parameters.

4.1. Optimization problem formulation

The formulation of the optimization problem is based on an evolutionary algorithm procedure. All the powertrain design and control parameters considered in this study are stored as genes of the chromosome vector **X**, as presented in Eq. (45).

$$\begin{aligned} [\mathbf{X}]_{1\times 279} = [&Q_{nomF}\ V_{nomF}\ T_{maxF}\ \omega_{TcF}\ Q_{nomR}\ V_{nomR}\ T_{maxR}\ \omega_{TcR} \cdots \\ &Cap_F\ Cap_R\ N_{sF}\ N_{sR}\ N_{pF}\ N_{pR}\ N_d\ \Delta V_F\ \Delta V_R\ SoC_{regF}\ SoC_{regR} \cdots \\ &\mathbf{MF_{PS}}\ \mathbf{RW_{PS}} \cdots \mathbf{MF_{HS(F)}}\ \mathbf{MF_{HS(R)}}\ \mathbf{RW_{HS(F)}}\ \mathbf{RW_{HS(R)}}] \end{aligned} \tag{45}$$

As mentioned previously, vehicle autonomy is still one of the major challenges regarding EV market expansion. Hence, the maximization of driving range D_R [km] is considered as the first optimization criterion f_1, as expressed by Eq. (46).

$$f_1(\mathbf{X}) = \max\Big(D_R(\mathbf{X})\Big) \tag{46}$$

Another essential drawback associated with electrified powertrain architectures is that extended-range EVs cause a significant increase in the vehicle's overall mass due to the use of large onboard energy storage systems. To address such a trade-off problem, the second optimization criterion f_2 is focused on the minimization of the HESS size, as shown in Eq. (47).

$$f_2(\mathbf{X}) = \min\Big(\ M_{bat(F)}(\mathbf{X}) + M_{bat(R)}(\mathbf{X})\ + M_{cap(F)}(\mathbf{X}) + M_{cap(R)}(\mathbf{X})\ \Big) \tag{47}$$

The last optimization criterion f_3 maximizes the battery state of health SoH. In this case, both rear and front battery packs are subjected to a 3000-h cycling process, in which the lowest $SoH_{(F/R)}$ is considered to be maximized by the genetic algorithm.

$$f_3(\mathbf{X}) = \max\Big(\min\Big(SoH_F(\mathbf{X}), SoH_R(\mathbf{X})\Big)\Big) \tag{48}$$

Finally, the optimization procedure is subjected to the fuzzy constraints C_{fuzzy} (see Eq. (37)) and the design constraints expressed by Eq. (49). A minimum correlation coefficient $COR_{min}(\mathbf{X})$ is established as one of the optimization constraints to avoid EV configurations with poor acceleration performance. Such parameter is determined by Eq. (50) according to the comparison between the target speed V_c and actual vehicle speed V.

$$C(\mathbf{X}) = \begin{cases} 20 \text{ Ah} \leq Q_{nom(F/R)} \leq 150 \text{ Ah} \\ 100 \text{ V} \leq V_{nom(F/R)} \leq 400 \text{ V} \\ 1 \leq N_{s(F/R)} \leq 25 \\ 1 \leq N_{p(F/R)} \leq 5 \\ 50 \text{ Nm} \leq T_{maxF} \leq 300 \text{ Nm} \\ 26 \text{ rad/s} \leq \omega_{TcF} \leq 314 \text{ rad/s} \\ 26 \text{ rad/s} \leq \omega_{TcR} \leq 209 \text{ rad/s} \\ 3.5 \leq N_d \leq 7 \\ 35\% \leq SoC_{reg(F/R)} \leq 95\% \\ V_{Ceq(F/R)} \leq V_{nom(F/R)} \\ COR_{min}(\mathbf{X}) \geq 0.99 \\ D_R \geq 94 \text{ km} \end{cases} \tag{49}$$

$$COR = \sqrt{\frac{\left(\sum \left(V_c - \bar{V}_c\right)\left(V - \bar{V}\right)\right)^2}{\sum \left(V_c - \bar{V}_c\right)^2 \sum \left(V - \bar{V}\right)^2}} \tag{50}$$

4.2. Interactive adaptive-weight genetic algorithm (i-AWGA)

In this work, the i-AWGA technique proposed by Gen et al. [136] solves the optimization problem. This genetic algorithm procedure was used since it has been successfully employed in previous works with regard to the multi-objective optimization of different complex systems such as plug-in hybrid electric vehicle powertrain [94,95], hydraulic hybrid vehicle powertrain [137–139], pure electric vehicle powertrain [32,63], multi-speed gearbox design [89,140] and gear shifting control [86,90]. Furthermore, the i-AWGA approach extensively searches for the most compromised solution, which is not limited to local optimal points. Moreover, this method was compared with

results reached by the particle swarm optimization (PSO) in previous works [125], and the results reached were similar.

The population members are classified according to the i-AWGA fitness function Ft presented in Eq. (51), which takes in account the maximum f_k^{min} and minimum f_k^{max} results for each optimization criterion. In addition, a penalty factor P_p is added to the fitness calculation, in which $P_p = 1$ for the first ranked members and $P_p = 0$ otherwise.

$$Ft(\mathbf{X}) = \frac{f_1(\mathbf{X}) - f_1^{min}}{f_1^{max} - f_1^{min}} + \frac{f_2^{max} - f_2(\mathbf{X})}{f_2^{max} - f_2^{min}} + \frac{f_3(\mathbf{X}) - f_3^{min}}{f_3^{max} - f_3^{min}} + P_p(\mathbf{X}) \tag{51}$$

In this sense, this technique weighs the importance of each optimization criterion and increases the chance of crossover/mutation of the best candidates, narrowing the evolutive process. The candidate that presents the highest fitness will also have the most significant selection probability S_P (Eq. (52)), which is determined based on the roulette wheel technique as a function of the population size P_{size}.

$$S_P(\mathbf{X}) = \frac{Ft(\mathbf{X})}{\sum_{X=1}^{P_{size}} Ft(\mathbf{X})} \tag{52}$$

During each generation, 20 pairs of chromosomes ($\mathbf{X}_1$ and $\mathbf{X}_2$) are selected to be randomly combined by the crossover process, thereby resulting in a new chromosome $\mathbf{X}_{cr}$. The combined member $\mathbf{X}_{cr}$ is afterward simulated and added to the current population, provided that this configuration meets the optimization constraints. In this case, there is an equal probability of selecting the design variables from both $\mathbf{X}_1$ and $\mathbf{X}_2$.

Moreover, to guarantee diversity of the population, a mutation operator is introduced, following the rules presented in Table 5. The design parameters of the chromosomes $\mathbf{X}_1$, $\mathbf{X}_2$ and $\mathbf{X}_{cr}$ are randomly mutated (with the probability of 50% [90,94]), which results in the new members $\mathbf{X}_{M1}$, $\mathbf{X}_{M2}$ and $\mathbf{X}_{Mcr}$, respectively. Those chromosomes are then simulated, evaluated based on the established constraints, and introduced into the population if the minimum performance factors were achieved.

Finally, the population size is limited by a maximum number of members ($P_{limit} = 200$). The highest Pareto ranked solutions are discarded once the population exceeds such limit [141]. In case the Pareto frontier (that is, first ranked solutions) presents higher size than P_{limit}, the population size is reset by the condition of $P_{limit} = P_{limit}+100$, so that the elimination of the whole population can be avoided. The stagnation of the Pareto frontier for over 10 generations [142] represents the convergence of the evolutive process.

4.3. Solver procedure and computational cost

The flowchart presented in Fig. 7 shows the logic applied to solve the optimization process. As presented in Eq. (45), each potential solution comprises 279 design variables, representing the electric drivetrain, batteries, and ultracapacitors parameters and the fuzzy controllers' membership functions and rules.

In order to evaluate all results analyzed by the optimization criteria presented in Eqs. (46)–(48), the overall procedure is divided into three

Table 5
Mutation operator.

Design variable	Initial chromosome	Mutation operator $0 \geq Mt(j) \geq 1$		Mutated chromosome
j	$[\mathbf{X}]^T$	$MT(j) < 0.5$	$MT(j) \geq 0.5$	$[\mathbf{X}_{MT}]^T$
$j = 1$	Q_{nomF}	$Q_{mutF} = 0$	$-15 \leq Q_{mutF} \leq 15$	$Q_{nomF} + Q_{mutF}$
$j = 2$	V_{nomF}	$V_{mutF} = 0$	$-60 \leq V_{mutF} \leq 60$	$V_{nomF} + V_{mutF}$
$j = 3$	T_{maxF}	$T_{mutF} = 0$	$-50 \leq T_{mutF} \leq 50$	$T_{maxF} + T_{mutF}$
$j = 4$	ω_{TcF}	$\omega_{mutF} = 0$	$-500 \leq \omega_{mutF} \leq 500$	$\omega_{TcF} + \omega_{mutF}$
$j = 5$	Q_{nomR}	$Q_{mutR} = 0$	$-15 \leq Q_{mutR} \leq 15$	$Q_{nomR} + Q_{mutR}$
$j = 6$	V_{nomR}	$V_{mutR} = 0$	$-60 \leq V_{mutR} \leq 60$	$V_{nomR} + V_{mutR}$
$j = 7$	T_{maxR}	$T_{mutR} = 0$	$-15 \leq T_{mutR} \leq 15$	$T_{maxR} + T_{mutR}$
$j = 8$	ω_{TcR}	$\omega_{mutR} = 0$	$-300 \leq \omega_{mutR} \leq 300$	$\omega_{TcR} + \omega_{mutR}$
$j = 9$	Cap_F	$Cap_{mutF} = Cap_F$	integer $[1 \leq Cap_{mutF} \leq 16]$	Cap_{mutF}
$j = 10$	Cap_R	$Cap_{mutR} = Cap_R$	integer $[1 \leq Cap_{mutR} \leq 16]$	Cap_{mutR}
$j = 11$	N_{sF}	$N_{sFmut} = N_{sF}$	integer $[1 \leq N_{sFmut} \leq 25]$	N_{sFmut}
$j = 12$	N_{sR}	$N_{sRmut} = N_{sR}$	integer $[1 \leq N_{sRmut} \leq 25]$	N_{sRmut}
$j = 13$	N_{pF}	$N_{pFmut} = N_{pF}$	integer $[1 \leq N_{pFmut} \leq 5]$	N_{pFmut}
$j = 14$	N_{pR}	$N_{pRmut} = N_{pR}$	integer $[1 \leq N_{pRmut} \leq 5]$	N_{pRmut}
$j = 15$	N_d	$N_{dmut} = 0$	$-0.5 \leq N_{dmut} \leq 0.5$	$N_d + N_{dmut}$
$j = 16$	SoC_{regF}	$SoC_{regFmut} = 0$	$-0.15 \leq SoC_{regFmut} \leq 0.15$	$SoC_{regF} + SoC_{regFmut}$
$j = 17$	SoC_{regR}	$SoC_{regRmut} = 0$	$-0.15 \leq SoC_{regRmut} \leq 0.15$	$SoC_{regR} + SoC_{regRmut}$
$j = 18$	ΔV_F	$\Delta V_{Fmut} = 0$	$-0.15 \leq \Delta V_{Fmut} \leq 0.15$	$\Delta V_F + \Delta V_{Fmut}$
$j = 19$	ΔV_R	$\Delta V_{Rmut} = 0$	$-0.15 \leq \Delta V_{Rmut} \leq 0.15$	$\Delta V_R + \Delta V_{Rmut}$
$20 \leq j \leq 27$	$\mathbf{MF}_{\mathbf{PS}_{(j-19)}}$	$\mathbf{MF}_{\mathbf{PS}_{mut(j-19)}} = \mathbf{MF}_{\mathbf{PS}_{(j-19)}}$	$-150 \leq \mathbf{MF}_{\mathbf{PS}_{mut(j-19)}} \leq 150$	$\mathbf{MF}_{\mathbf{PS}_{(j-19)}} + \mathbf{MF}_{\mathbf{PS}_{mut(j-19)}}$
$28 \leq j \leq 35$	$\mathbf{MF}_{\mathbf{PS}_{(j-27)}}$	$\mathbf{MF}_{\mathbf{PS}_{mut(j-27)}} = \mathbf{MF}_{\mathbf{PS}_{(j-27)}}$	$-0.1 \leq \mathbf{MF}_{\mathbf{PS}_{mut(j-27)}} \leq 0.1$	$\mathbf{MF}_{\mathbf{PS}_{(j-27)}} + \mathbf{MF}_{\mathbf{PS}_{mut(j-27)}}$
$36 \leq j \leq 43$	$\mathbf{MF}_{\mathbf{PS}_{(j-35)}}$	$\mathbf{MF}_{\mathbf{PS}_{mut(j-35)}} = \mathbf{MF}_{\mathbf{PS}_{(j-35)}}$	$-0.1 \leq \mathbf{MF}_{\mathbf{PS}_{mut(j-35)}} \leq 0.1$	$\mathbf{MF}_{\mathbf{PS}_{(j-35)}} + \mathbf{MF}_{\mathbf{PS}_{mut(j-35)}}$
$44 \leq j \leq 51$	$\mathbf{MF}_{\mathbf{PS}_{(j-43)}}$	$\mathbf{MF}_{\mathbf{PS}_{mut(j-43)}} = \mathbf{MF}_{\mathbf{PS}_{(j-43)}}$	$-0.1 \leq \mathbf{MF}_{\mathbf{PS}_{mut(j-43)}} \leq 0.1$	$\mathbf{MF}_{\mathbf{PS}_{(j-43)}} + \mathbf{MF}_{\mathbf{PS}_{mut(j-43)}}$
$52 \leq j \leq 78$	$\mathbf{RW}_{\mathbf{PS}_{(j-51)}}$	$\mathbf{RW}_{\mathbf{PS}_{mut(j-51)}} = \mathbf{RW}_{\mathbf{PS}_{(j-51)}}$	integer $[1 \leq \mathbf{RW}_{\mathbf{PS}_{mut(j-51)}} \leq 3]$	$\mathbf{RW}_{\mathbf{PS}_{mut(j-51)}}$
$79 \leq j \leq 105$	$\mathbf{RW}_{\mathbf{PS}_{(j-78)}}$	$\mathbf{RW}_{\mathbf{PS}_{mut(j-78)}} = \mathbf{RW}_{\mathbf{PS}_{(j-78)}}$	$0 \leq \mathbf{RW}_{\mathbf{PS}_{mut(j-78)}} \leq 1$	$\mathbf{RW}_{\mathbf{PS}_{mut(j-78)}}$
$106 \leq j \leq 113$	$\mathbf{MF}_{\mathbf{HS(F)}_{(j-105)}}$	$\mathbf{MF}_{\mathbf{HS(F)}_{mut(j-105)}} = \mathbf{MF}_{\mathbf{HS(F)}_{(j-105)}}$	$-250 \leq \mathbf{MF}_{\mathbf{HS(F)}_{mut(j-105)}} \leq 250$	$\mathbf{MF}_{\mathbf{HS(F)}_{(j-105)}} + \mathbf{MF}_{\mathbf{HS(F)}_{mut(j-105)}}$
$114 \leq j \leq 121$	$\mathbf{MF}_{\mathbf{HS(F)}_{(j-113)}}$	$\mathbf{MF}_{\mathbf{HS(F)}_{mut(j-113)}} = \mathbf{MF}_{\mathbf{HS(F)}_{(j-113)}}$	$-0.1 \leq \mathbf{MF}_{\mathbf{HS(F)}_{mut(j-113)}} \leq 0.1$	$\mathbf{MF}_{\mathbf{HS(F)}_{(j-113)}} + \mathbf{MF}_{\mathbf{HS(F)}_{mut(j-113)}}$
$122 \leq j \leq 129$	$\mathbf{MF}_{\mathbf{HS(F)}_{(j-121)}}$	$\mathbf{MF}_{\mathbf{HS(F)}_{mut(j-121)}} = \mathbf{MF}_{\mathbf{HS(F)}_{(j-121)}}$	$-0.1 \leq \mathbf{MF}_{\mathbf{HS(F)}_{mut(j-121)}} \leq 0.1$	$\mathbf{MF}_{\mathbf{HS(F)}_{(j-121)}} + \mathbf{MF}_{\mathbf{HS(F)}_{mut(j-121)}}$
$130 \leq j \leq 137$	$\mathbf{MF}_{\mathbf{HS(F)}_{(j-129)}}$	$\mathbf{MF}_{\mathbf{HS(F)}_{mut(j-129)}} = \mathbf{MF}_{\mathbf{HS(F)}_{(j-129)}}$	$-0.1 \leq \mathbf{MF}_{\mathbf{HS(F)}_{mut(j-129)}} \leq 0.1$	$\mathbf{MF}_{\mathbf{HS(F)}_{(j-129)}} + \mathbf{MF}_{\mathbf{HS(F)}_{mut(j-129)}}$
$138 \leq j \leq 145$	$\mathbf{MF}_{\mathbf{HS(R)}_{(j-137)}}$	$\mathbf{MF}_{\mathbf{HS(R)}_{mut(j-137)}} = \mathbf{MF}_{\mathbf{HS(R)}_{(j-137)}}$	$-250 \leq \mathbf{MF}_{\mathbf{HS(R)}_{mut(j-137)}} \leq 250$	$\mathbf{MF}_{\mathbf{HS(R)}_{(j-137)}} + \mathbf{MF}_{\mathbf{HS(R)}_{mut(j-137)}}$
$146 \leq j \leq 153$	$\mathbf{MF}_{\mathbf{HS(R)}_{(j-145)}}$	$\mathbf{MF}_{\mathbf{HS(R)}_{mut(j-145)}} = \mathbf{MF}_{\mathbf{HS(R)}_{(j-145)}}$	$-0.1 \leq \mathbf{MF}_{\mathbf{HS(R)}_{mut(j-145)}} \leq 0.1$	$\mathbf{MF}_{\mathbf{HS(R)}_{(j-145)}} + \mathbf{MF}_{\mathbf{HS(R)}_{mut(j-145)}}$
$154 \leq j \leq 161$	$\mathbf{MF}_{\mathbf{HS(R)}_{(j-153)}}$	$\mathbf{MF}_{\mathbf{HS(R)}_{mut(j-153)}} = \mathbf{MF}_{\mathbf{HS(R)}_{(j-153)}}$	$-0.1 \leq \mathbf{MF}_{\mathbf{HS(R)}_{mut(j-153)}} \leq 0.1$	$\mathbf{MF}_{\mathbf{HS(R)}_{(j-153)}} + \mathbf{MF}_{\mathbf{HS(R)}_{mut(j-153)}}$
$162 \leq j \leq 169$	$\mathbf{MF}_{\mathbf{HS(R)}_{(j-161)}}$	$\mathbf{MF}_{\mathbf{HS(R)}_{mut(j-161)}} = \mathbf{MF}_{\mathbf{HS(R)}_{(j-161)}}$	$-0.1 \leq \mathbf{MF}_{\mathbf{HS(R)}_{mut(j-161)}} \leq 0.1$	$\mathbf{MF}_{\mathbf{HS(R)}_{(j-161)}} + \mathbf{MF}_{\mathbf{HS(R)}_{mut(j-161)}}$
$170 \leq j \leq 196$	$\mathbf{RW}_{\mathbf{HS(F)}_{(j-169)}}$	$\mathbf{RW}_{\mathbf{HS(F)}_{mut(j-169)}} = \mathbf{RW}_{\mathbf{HS(F)}_{(j-169)}}$	integer $[1 \leq \mathbf{RW}_{\mathbf{HS(F)}_{mut(j-169)}} \leq 3]$	$\mathbf{RW}_{\mathbf{HS(F)}_{mut(j-169)}}$
$197 \leq j \leq 223$	$\mathbf{RW}_{\mathbf{HS(F)}_{(j-196)}}$	$\mathbf{RW}_{\mathbf{HS(F)}_{mut(j-196)}} = \mathbf{RW}_{\mathbf{HS(F)}_{(j-196)}}$	$0 \leq \mathbf{RW}_{\mathbf{HS(F)}_{mut(j-196)}} \leq 1$	$\mathbf{RW}_{\mathbf{HS(F)}_{mut(j-196)}}$
$j = 224$	$\mathbf{RW}_{\mathbf{HS(F)}_{(j-223)}}$	$\mathbf{RW}_{\mathbf{HS(F)}_{mut(j-223)}} = \mathbf{RW}_{\mathbf{HS(F)}_{(j-223)}}$	integer $[1 \leq \mathbf{RW}_{\mathbf{HS(F)}_{mut(j-223)}} \leq 5]$	$\mathbf{RW}_{\mathbf{HS(F)}_{mut(j-223)}}$
$225 \leq j \leq 251$	$\mathbf{RW}_{\mathbf{HS(R)}_{(j-224)}}$	$\mathbf{RW}_{\mathbf{HS(R)}_{mut(j-224)}} = \mathbf{RW}_{\mathbf{HS(R)}_{(j-224)}}$	integer $[1 \leq \mathbf{RW}_{\mathbf{HS(R)}_{mut(j-224)}} \leq 3]$	$\mathbf{RW}_{\mathbf{HS(R)}_{mut(j-224)}}$
$252 \leq j \leq 278$	$\mathbf{RW}_{\mathbf{HS(R)}_{(j-251)}}$	$\mathbf{RW}_{\mathbf{HS(R)}_{mut(j-251)}} = \mathbf{RW}_{\mathbf{HS(R)}_{(j-251)}}$	$0 \leq \mathbf{RW}_{\mathbf{HS(R)}_{mut(j-251)}} \leq 1$	$\mathbf{RW}_{\mathbf{HS(R)}_{mut(j-251)}}$
$j = 279$	$\mathbf{RW}_{\mathbf{HS(R)}_{(j-278)}}$	$\mathbf{RW}_{\mathbf{HS(R)}_{mut(j-278)}} = \mathbf{RW}_{\mathbf{HS(R)}_{(j-278)}}$	integer $[1 \leq \mathbf{RW}_{\mathbf{HS(R)}_{mut(j-278)}} \leq 5]$	$\mathbf{RW}_{\mathbf{HS(R)}_{mut(j-278)}}$

main simulation stages. The first one is the vehicle longitudinal dynamics model, in which the EV performance and batteries SoC_B regime are defined. In this stage, the component masses required to define the f_2 optimization criteria are calculated according to the chromosome parameters. Moreover, the vehicle drive range (f_1) is defined as the traveled distance of the EV simulation, repeating the driving cycles (Fig. 2) until one of the batteries reaches $SoC_B = 40\%$. Two more simulation stages were required to define the batteries' SoH, the third optimization criterion (f_3). Based on the battery parameters and final SoC_B retrieved from the longitudinal dynamics simulation, the batteries' plug-in charging is performed to define the current profile applied in the charging procedure. Unlike the first simulation stage in which the overall EV is simulated, the battery recharging needs to be performed in individual simulations, mainly due to each battery's different characteristics and different charging times. Finally, the discharging current profile from the first stage is combined with the second simulation stage's recharging profile. The batteries were evaluated considering a 3000-h cycle replicating the charging regime. In the same way as the recharging simulation, the battery SoH evaluation also needs to be performed in individual simulations for each battery.

With the simulated results of each valid chromosome, the i-AWGA method is applied. First, the population Ft values are updated, and the crossover and mutation operators are applied. The valid chromosomes which attempt the constraints are then added to the population to be simulated in the next generation. Finally, this process is repeated until the algorithm reaches its convergence criterion.

Once the simulation time varies according to the EV characteristics and reaches the driving range, the processing time also changes. Table 6 shows the processing time of some case analyses in the current paper, considering the minimum and maximum processing time for each simulation stage. Moreover, the computational cost of the battery end of life ($SoH = 0.8$) is also presented. However, due to its long processing time, it is only performed for some selected solutions in the results analyses section.

The simulations were performed on a computer equipped with an Intel i7 processor (3.20 GHz) with 16 Gb RAM. Considering the overall optimization procedure, running five simultaneous simulations in parallel was possible. Three similar computers were used to process the GA optimization, totalizing 15 parallel simulations. The algorithm runs for 458 generations, considering 80 novel solutions per generation. The final processing time was about 278.19 h, which is reasonable considering the high number of design variables and the high complexity of the simulated models.

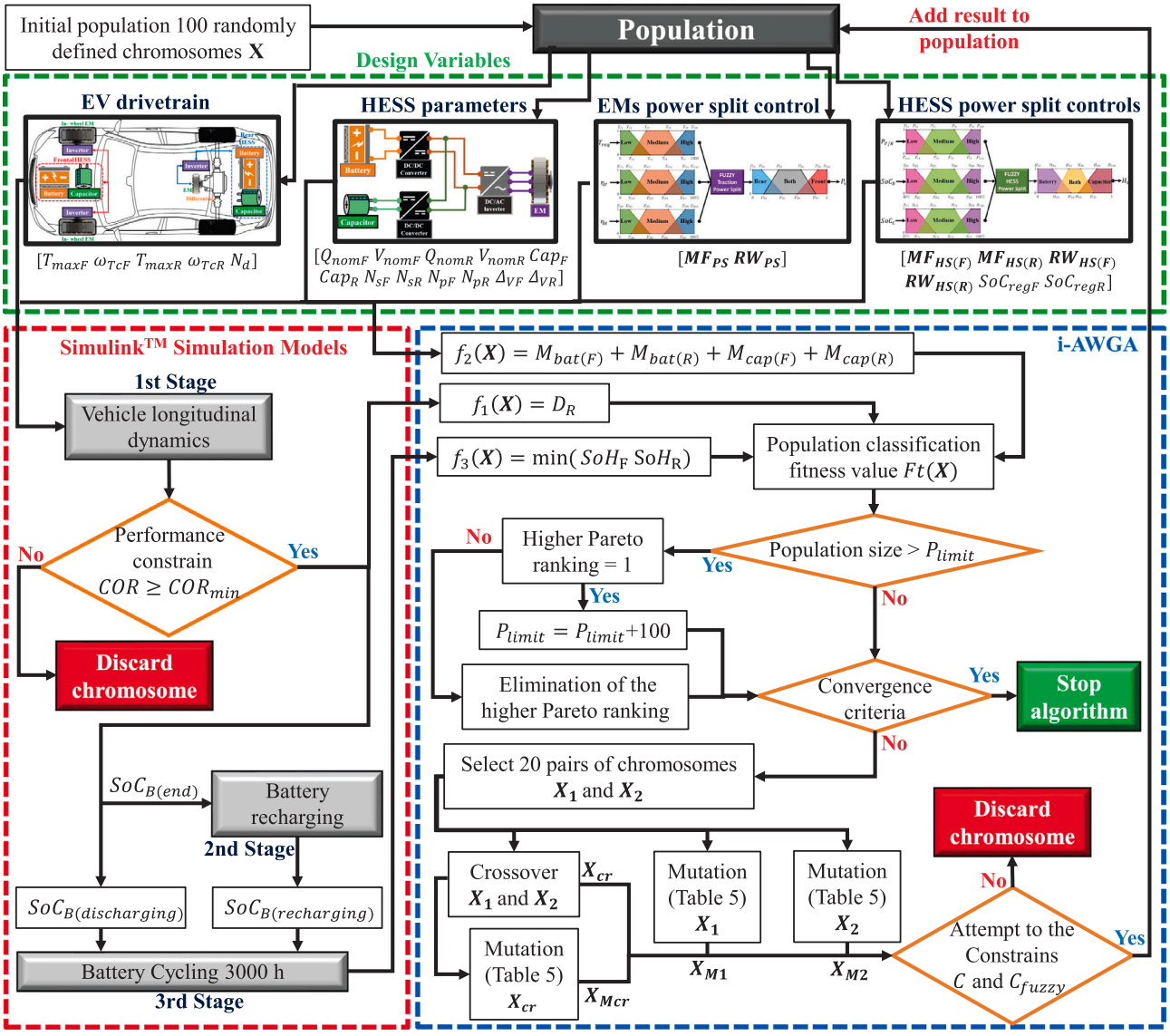

Fig. 7. Optimization procedure flowchart.

Table 6
Simulation time for each optimization step.

Stage	Simulated parameters	Simulated time		Processing time	
		Minimum	Maximum	Minimum	Maximum
1	Longitudinal dynamics	1.98 h ($D_R \approx 98$ km)	7.19 h ($D_R \approx 369$ km)	163.43 s	577.36 s
2	Battery recharging	2.15 h $Q_{nom} \approx 135$ Ah, $V_{nom} \approx 300$ V	2.47 h $Q_{nom} \approx 34$ Ah, $V_{nom} \approx 126$ V	1.35 s	1.70 s
3	Battery cycling (SoH)	3000 h		38.07 s	
- - -	Battery end of life ($SoH = 0.8$)	10 012 h SoH (3000 h) = 0.9708	65 562 h SoH (3000 h) = 0.9930	200.19 s	788.58 s

5. Optimization results and discussion

After convergence, the Pareto frontier of non-dominated solutions is defined as optimum Dual-HESS EV configurations. Among these, the best configurations regarding each optimization criteria, maximum driving range ($\max f_1$), minimum HESS mass ($\min f_2$), and maximum battery state of health SoH ($\max f_3$), were selected to be analyzed. Moreover, the solution that presents the best trade-off among the optimization criteria, characterized by the highest fitness function value ($\max Ft$), is also included in the analyses of the results. Fig. 8 shows the Pareto frontier, and Table 7 presents the results of the selected solutions and the critical design variables of their chromosomes.

The $\max f_1$ solution reaches a driving range of over 369 km with two heavy HESSs, adding up to 566 kg to the vehicle. This configuration relies on two high capacity batteries –134.71 Ah, 300.25 V at the front and 110.1 Ah, 328.28 V at the rear, HESS - both with 16 V capacitors assembled only in series with their respective batteries. Once these batteries are large, they are robust to deep discharges, ensuring a lifespan of 44 412 h and 43 450 h for the frontal and rear batteries, respectively. Regarding the drivetrain, the $\max f_1$ EV configuration presents a rear EM with higher torque as compared to the other selected solutions (see Table 7) to ensure acceptable performance, especially at the EV startup, even considering it higher total mass. Besides the listed advantages, the $\max f_1$ solution represents a high overall powertrain cost, which will be discussed in detail in Section 5.2.

On the other hand, the $\min f_2$ solution presents the small HESS pack combination, with an overall 132.77 kg energy storage mass. This EV configuration presents a smaller driving range of 98.34 km,

Table 7
Dual HESS EV optimized result.

Results	Dual HESS EV solutions			
	Max. driving range $\max(f_1)$	Min. HESS mass $\min(f_2)$	Max. battery life $\max(f_3)$	Best trade-off $\max(Ft)$
Driving range [km]	369.16	98.34	223.98	285.56
Performance $COR(X)$	0.9937	0.9922	0.9912	0.9903
$M_{bat(F)}$ [kg]	269.63	62.24	254.29	214.76
$M_{bat(R)}$ [kg]	240.95	28.54	83.78	75.58
$M_{cap(F)}$ [kg]	27	21	28.7	21
$M_{cap(R)}$ [kg]	28.7	21	107.1	21
SoH_F	0.9917	0.9708	0.9927	0.9881
Front battery life [h]	44 412	10 012	54 133	36 585
Front battery life [cycles]	6174	5054	12 224	6359
SoH_R	0.9913	0.9734	0.9930	0.9884
Rear battery life [h]	43 450	10 203	65 562	38 201
Rear battery life [cycles]	6040	5150	14 805	6641
Final $SoC_{B(F)}$ (front) [%]	45.69	40	40	40
Final $SoC_{B(R)}$ (rear) [%]	40	43.88	69.36	50.13
Final $SoC_{C(F)}$ (front) [%]	67.45	77.29	36.81	38.61
Final $SoC_{C(R)}$ (rear) [%]	35.73	37.81	42.67	32.86
Recharging time (front) C_{tF} [h]	2.15	2.47	2.44	2.41
Recharging time (rear) C_{tR} [h]	2.36	2.38	1.24	2.07
$\frac{\text{Driving Range}}{\text{Energy storage mass}}$ [km/kg]	0.6519	0.7406	0.4727	0.8592
Chromosomes				
Q_{nomF} [Ah]	134.71	53.47	105.69	132.75
V_{nomF} [V]	300.25	174.59	360.9	242.67
T_{maxF} [Nm]	178.77	179.61	195.86	197.17
ω_{TcF} [rpm]	293.1	294.42	327.04	294.09
Q_{nomR} [Ah]	110.1	33.99	52.71	70.51
V_{nomR} [V]	328.28	125.91	238.44	160.79
T_{maxR} [Nm]	82.26	30.62	41.26	28.67
ω_{TcR} [rpm]	1062.91	1062.91	1018.28	1062.91
Cap_F	1	1	3	1
Cap_R	3	1	5	1
N_{sF}	9	7	7	7
N_{sR}	7	7	7	7
N_{pF}	1	1	1	1
N_{pR}	1	1	3	1
N_d	3.84	3.86	5.27	4.17
SoC_{regF} [%]	82.31	82.31	46.08	57.36
SoC_{regR} [%]	39.69	40.68	44.68	37.86
ΔV_F	1.89	1.75	1.99	1.96
ΔV_R	1.90	1.98	1.85	1.94

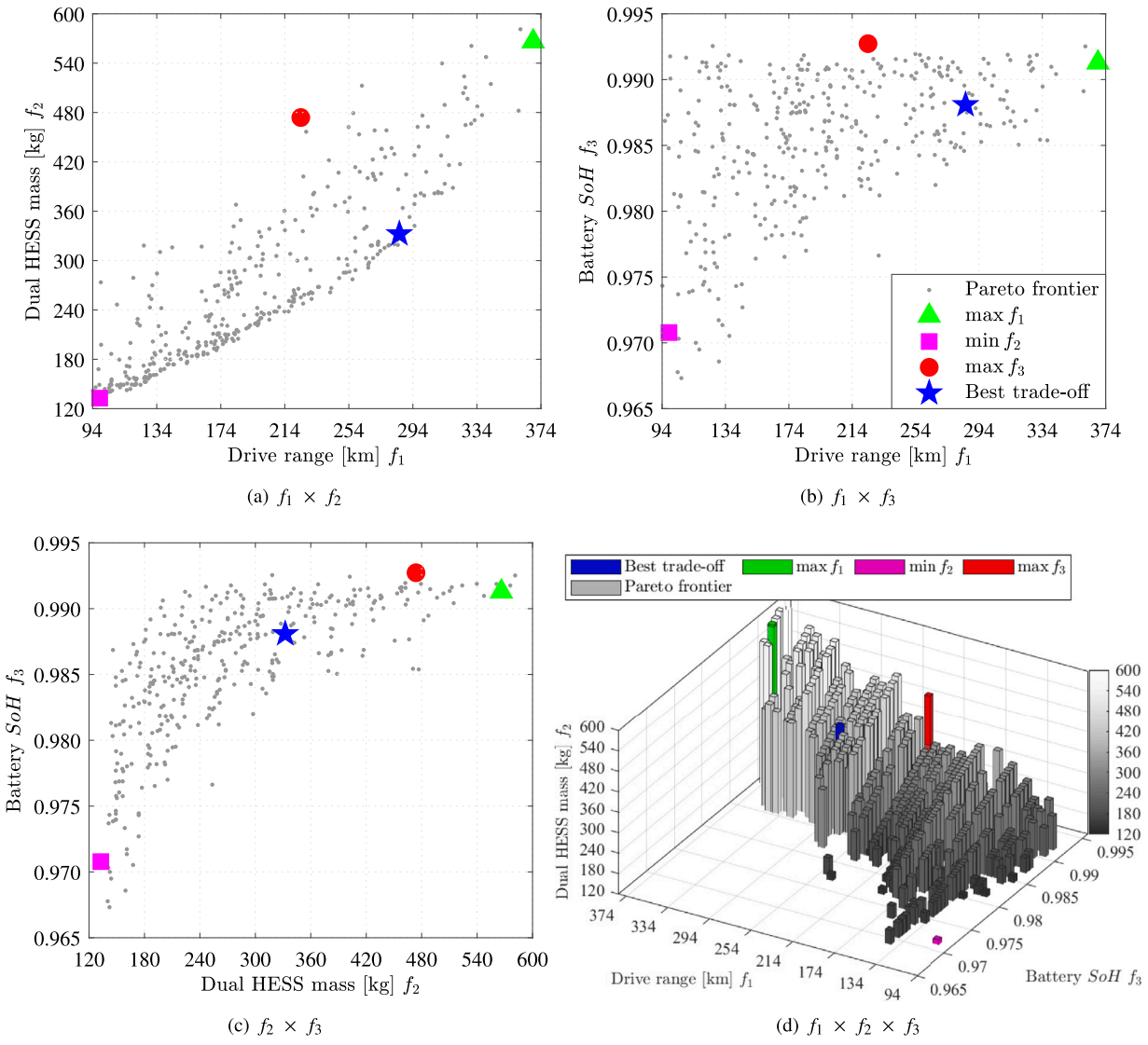

Fig. 8. Optimized solutions.

close to the minimum allowed 2 loops in the analyzed driving cycle. The lower power of the min f_2 solution (53.47 Ah 174.59 V at the front and 33.62 Ah 125.91 V at the rear HESS) associated in the both HESS with the smaller 16 V ultracapacitors assembled only in the series configuration. Therefore, these HESSs are cheaper, but, at the same time, they are stressed with deeper discharges, resulting in a life cycle of only 10 012 h and 10 203 h for the frontal and rear systems, respectively.

Considering the battery life cycle, the max f_3 Dual HESS EV presents the most extended cycle with 54 133 h and 65 562 h for the frontal and rear HESSs. This EV reaches 223.98 km range with a higher voltage HESS than the other analyzed solutions. Another significant difference is the use of greater ultracapacitors (but keeping the 16 V models) and the use of a 3 parallel capacitor assembled in the rear HESS, which saves the rear battery SoC, avoiding deep discharges even considering its lower capacity (52.71 Ah) as compared to the frontal HESS (105.69 Ah). Fig. 9 shows the analyzed Dual HESS EV batteries SoC during the simulated driving cycles, in which it is possible to observe that the max f_3 configuration keeps the large SoC gap between the frontal and rear HESS, even considering that the final SoH values are almost similar −0.9927 and 0.9930, respectively. However, due to its extra protection for batteries discharges, the max f_3 configuration presented the worst driving range per energy storage mass ratio as shown in Table 7.

Finally, the best trade-off solution (max Ft) was able to reach a 285.56 km driving range with a 332.34 kg overall energy storage system, which represents the best range by mass ratio among the analyzed solutions (see Table 7). The max Ft solution combines two HESS with different characteristics, (similar to the max f_3 architecture). The frontal HESS presents a high capacity battery (242.67 V, 132.75 Ah) combined with only series 16 V ultracapacitors arrangement. On the other hand, the rear HESS comprises a 160.79 V, 70.51 Ah battery connected in series with the smallest available 16 V ultracapacitors. Due to this gap between the frontal and rear batteries size, the power management control also does not discharge the rear battery to $SoC = 40\%$ (see Fig. 9) to keep its SoH close to that of the frontal battery, resulting in 36 585 h life cycle for the frontal battery and 38 201 h for the rear one. The relation among battery mass, SoC, and SoH of the selected Dual HESS EV configuration is presented in Fig. 10.

Even considering that the best trade-off solution presents a battery life lower than the max f_1 and the max f_3 solutions (see Table 7), the max Ft Dual HESS EV configuration powertrain is cheaper than the other ones. The following section provides the cost analysis of the selected configuration and a benchmark comparison with other solutions presented in the literature.

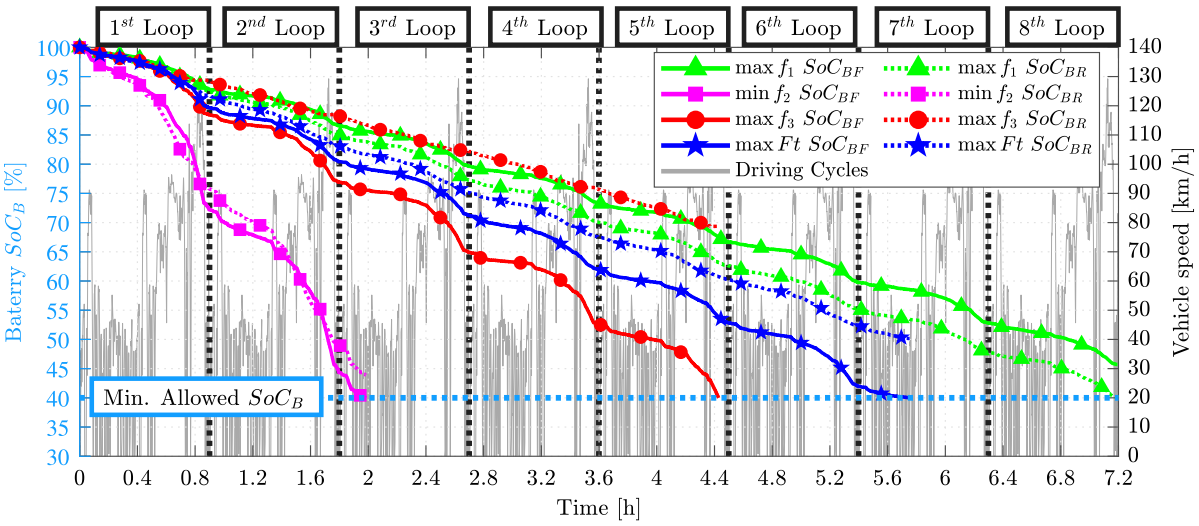

Fig. 9. Battery SoC_B of the optimum Dual HESS EV solutions.

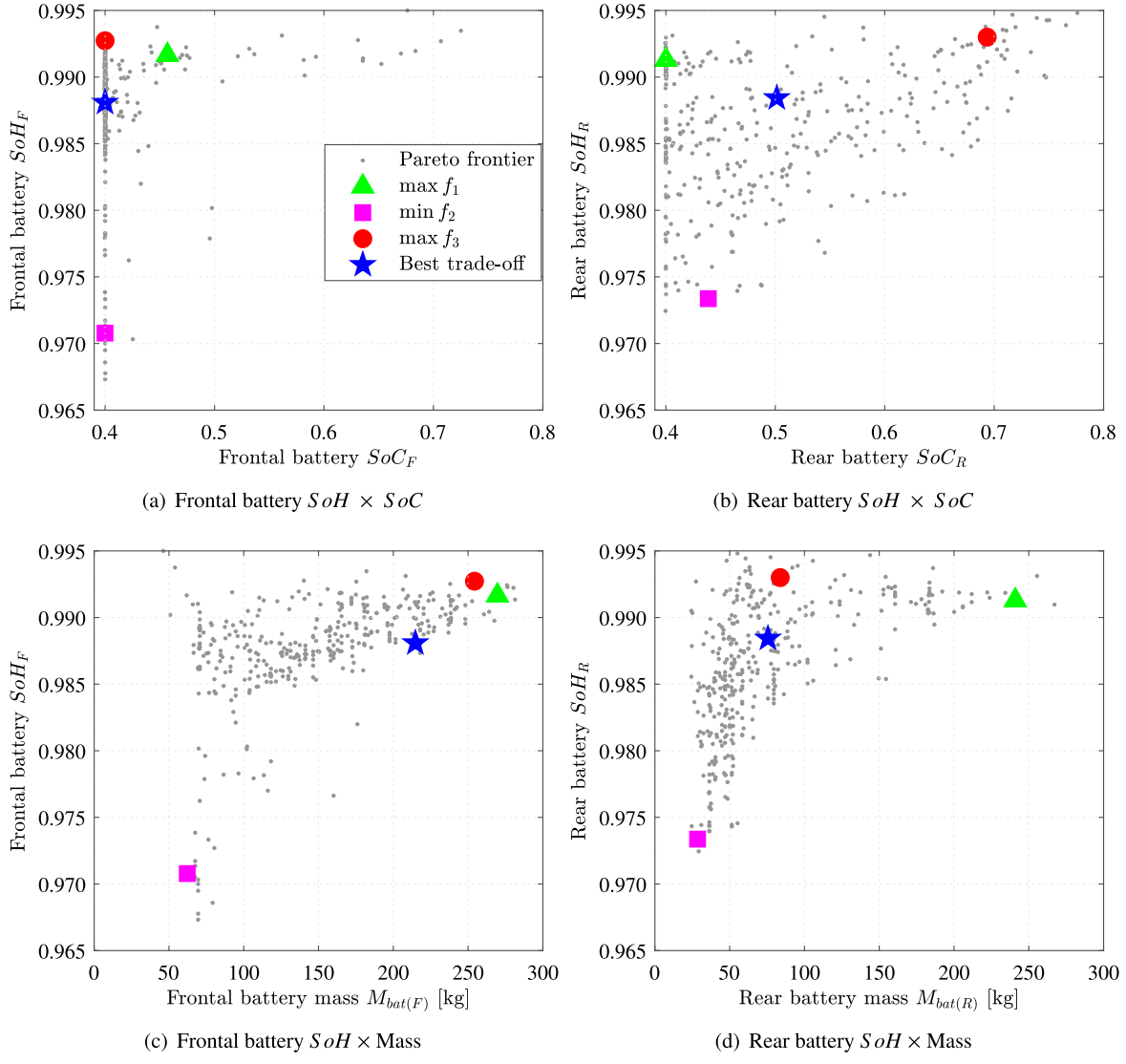

(a) Frontal battery $SoH \times SoC$

(b) Rear battery $SoH \times SoC$

(c) Frontal battery $SoH \times$ Mass

(d) Rear battery $SoH \times$ Mass

Fig. 10. Optimized solutions.

5.1. Single HESS comparison

In order to highlight the gains of the Dual-HESS EV topology, this section compares a similar EV powered by a single HESS. The single HESS EV presents the same propelling system architecture and fuzzy control scheme applied in the dual HESS. The only difference is that the single HESS EV frontal and rear drive systems are powered by the same HESS as shown in the diagram illustrated in Fig. 11. This single HESS EV is based on the exact vehicle used in the dual HESS. It is optimized under the same circumstances, considering only a single battery associated with an ultracapacitors pack. The overall EV drivetrain and respective power split and HESS current split controllers are also fully optimized to better fit the single HESS EV characteristics.

The single HESS EV design variables are listed in the $[\mathbf{X}_s]$ chromosome (Eq. (53)).

$$[\mathbf{X}_s]_{1\times 185} = [Q_{nom}\ V_{nom}\ T_{maxF}\ \omega_{TcF}\ T_{maxR}\ \omega_{TcR} \cdots \\ Cap\ N_s\ N_p\ N_d\ \Delta V\ SoC_{reg}\ \mathbf{MF_{PS}}\ \mathbf{RW_{PS}}\ \mathbf{MF_{HS}}\ \mathbf{RW_{HS}}] \quad (53)$$

The optimization procedure of the single HESS EV is based on the problem formulated in Section 4.1. However, the optimization criteria are updated to fit the Ev configuration with only one HESS.

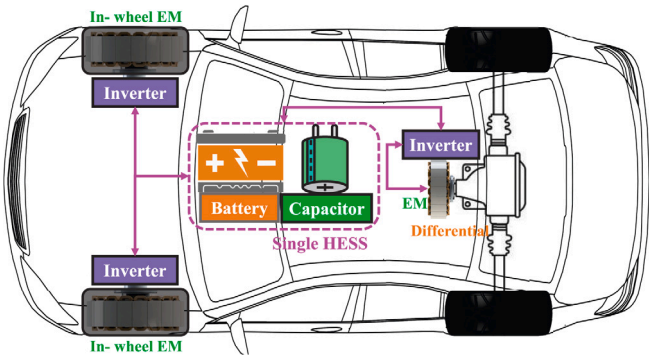

Fig. 11. Single HESS EV concept.

The constraints shown in Eq. (49) and the i-AWGA method presented in Section 4.2 are also applied for the single HESS optimization procedure.

$$f_1(\mathbf{X}_s) = \max\Big(D_R(\mathbf{X}_s)\Big) \quad (54)$$

$$f_2(\mathbf{X}_s) = \min\Big(M_{bat}(\mathbf{X}_s) + M_{cap}(\mathbf{X}_s)\Big) \quad (55)$$

$$f_3(\mathbf{X}_s) = \max\Big(SoH(\mathbf{X}_s)\Big) \quad (56)$$

Among the Pareto frontier reached by the optimizing of the single HESS EV, four solutions were selected to be compared to the dual HESS results, following the same criteria applied in the results shown in Table 7. The results and chromosomes reached by these single HESS solutions are presented in Table 8.

Fig. 12abc compares between the final Pareto frontier of non-dominated solutions reached by the dual and single HESS optimizations. It is possible to observe a break-even region for the analyzed EV configurations' drive range/energy storage mass ratio. The single HESS EV presents advantages for lower driving autonomy per energy storage mass ratios (94 km to 203 km Fig. 12a). In addition, the $\min f_2$ solution of the single HESS presents a driving range per HESS mass ratio of 0.8442 against the 0.7406 of the dual HESS. Moreover, the SoH value of the $\min f_2$ single HESS (0.9855) is far better than the reached values of the dual HESS (0.9708 - 0.9734).

Considering longer driving ranges, the dual HESS EV stands out. For the $\max f_1$ EV solutions, the dual HESS EV reached up to 369.16 km range against the 270.34 km reached by the single HESS. Regarding the best trade-off solutions, the dual HESS EV presents a better ratio between drive range and HESS mass (285.56 km/332.34 kg = 0.8592) as compared to the values achieved by the $\max Ft$ single HESS (238.82 km/286.32 kg = 0.8341), with similar values of battery SoH. However, considering the whole battery life cycle, $\max Ft$ dual HESS frontal and rear batteries increased their lifetime by 17.68% (5497 h) and 22.88% (7113 h), respectively, compared to the $\max Ft$ single HESS EV. Moreover, it is noteworthy to mention that the best trade-off dual HESS EV outperforms the driving range reached by the $\max f_1$ single HESS EV by 15 km.

Table 8
Single HESS EV optimized results.

Results	Single HESS EV solutions			
	Max. driving range $\max(f_1)$	Min. HESS mass $\min(f_2)$	Max. battery life $\max(f_3)$	Best trade-off $\max(Ft)$
Driving range [km]	270.34	98.25	256.46	238.82
Performance $COR(X)$	0.9942	0.9931	0.9912	0.9910
M_{bat} [kg]	364.43	95.38	369.28	265.31
M_{cap} [kg]	21	21	21	21
SoH	0.9908	0.9855	0.9924	0.9880
Battery life [h]	38 383	11 420	43 781	31 088
Battery life [cycles]	7221	5764	8489	6467
Final SoC_B [%]	40	40	40	40
Final SoC_C [%]	22.86	60.32	22.87	83.23
Recharging time C_{tF} [h]	2.40	2.46	2.40	2.41
$\frac{\text{Driving Range}}{\text{Energy storage mass}}$ [km/kg]	0.7014	0.8442	0.6571	0.8341
	Chromosomes			
Q_{nom} [Ah]	143.97	86.21	144.05	148.77
V_{nom} [V]	379.67	165.96	384.54	267.50
T_{maxF} [Nm]	234.78	217.70	231.30	220.87
ω_{TcF} [rpm]	304.75	293.09	297.53	294.09
T_{maxR} [Nm]	70.22	33.69	28.13	22.24
ω_{TcR} [rpm]	584.61	539.51	584.61	776.20
Cap	1	1	1	1
N_s	7	7	7	7
N_p	1	1	1	1
N_d	5.67	5.44	5.23	4.86
SoC_{reg} [%]	45.50	65.12	47.54	93.76
ΔV	1.93	1.80	1.99	1.96

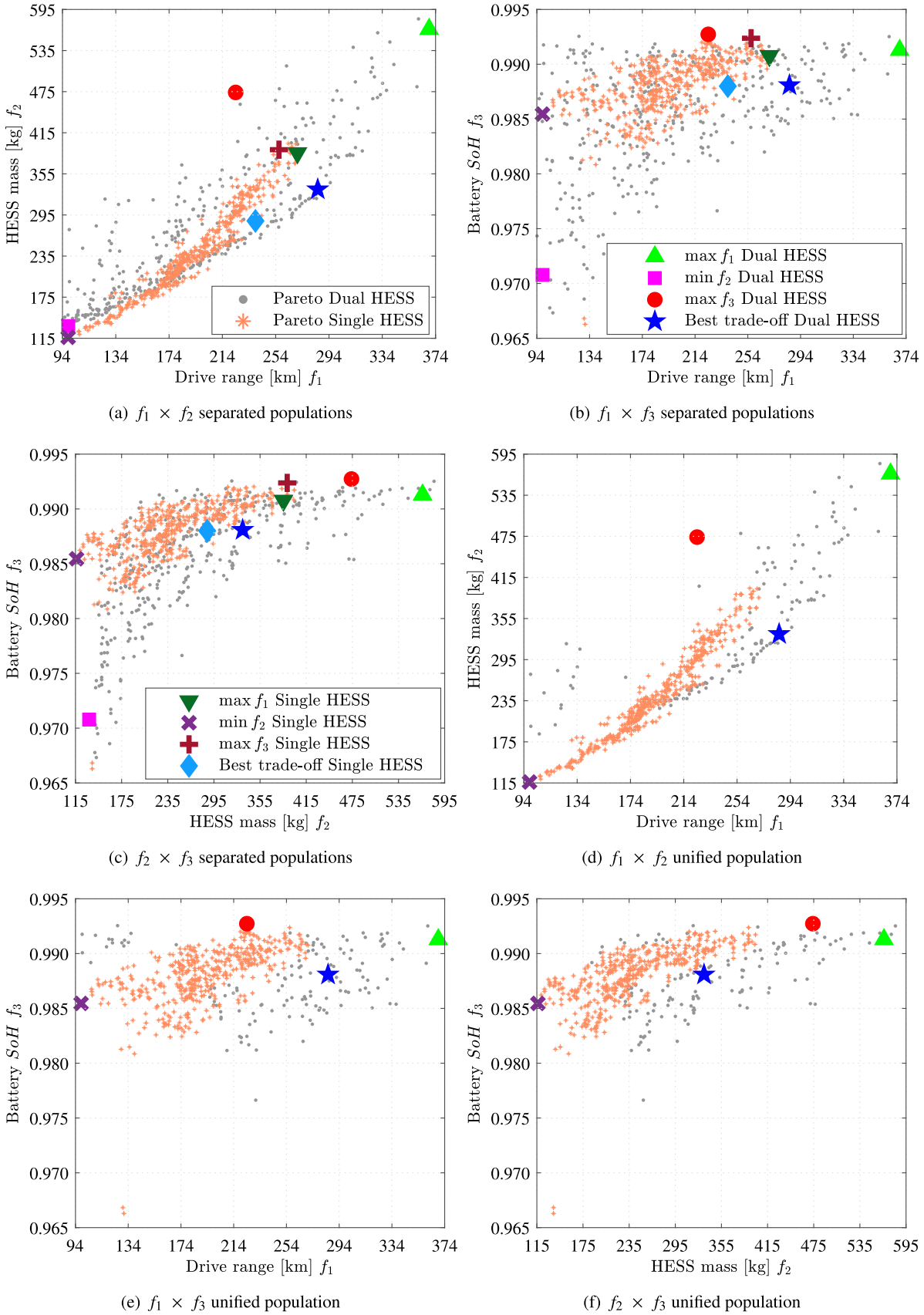

(a) $f_1 \times f_2$ separated populations

(b) $f_1 \times f_3$ separated populations

(c) $f_2 \times f_3$ separated populations

(d) $f_1 \times f_2$ unified population

(e) $f_1 \times f_3$ unified population

(f) $f_2 \times f_3$ unified population

Fig. 12. Comparison among single HESS and dual HESS EV Optimized solutions.

The advantages of the dual HESS EV configuration are more evident when both populations (single and dual HESS) are combined and the Pareto frontier and fitness values (Eq. (51)) recalculated. The combined population Pareto frontier is presented in Fig. 12def. As mentioned before, the single HESS EV is better for lower driving ranges, up to 203 km, while between 203 km and ≈ 260 km, both EV topologies show advantages. Additionally, the dual HESS configurations present a better drive range by HESS mass ratio and the single HESS EVs show higher values of battery SoH, except the max f_3 dual HESS EV that still presents the higher SoH values mainly due to its large batteries and unfavorable range per mass ratio (223.98 km/473.83 kg = 0.4727). For driving above 275 km, the population is composed only of dual HESS configurations, because these EVs hold bigger batteries, the SoH values increase at the same levels reached by the single HESS EVs.

Considering the unified population, it is possible to observe that the max f_1, max f_3 and max Ft still match the optimized dual HESS-based EV configurations previously analyzed. On the other hand, the min f_2 single HESS EV completely dominates the min f_2 dual HESS, eliminating it from the population. Finally, it is worth pointing out that the best trade-off single HESS solution was not eliminated in the unification process. However, it is only classified as the 76th out of 587 solutions. Therefore, based on the presented information, it is possible to conclude that the dual HESS EV configuration presents advantages as compared to the single HESS EV, under the analyzed scenarios. However, it is important to highlight that the gains presented in the current work are only possible due to the synergy reached by the optimization of the overall vehicle powertrain and control. Simply splitting the energy storage system in order to achieve a dual HESS EV, without optimizing the other vehicle components, will not generate significant improvements for the EV drive range, energy storage mass, or battery life.

5.2. Cost analysis

This section presents a comparative cost–benefit analysis between the optimal single and dual HESS-based EV configurations reached by the current work, and other optimized powertrain topologies achieved in previous works. Table 9 shows the financial results for each electrified propulsion technology. The results indicate that, despite the increase in the total cost of ownership for dual HESS EV configurations, the best trade-off solution for the proposed powertrain architecture outperformed both EHHV and single HESS EV cases for the range-to-cost ratio.

The overall costs of the propulsion systems for the best solutions were estimated and compared with a single HESS-based EV [63] and an EHHV (electric–hydraulic hybrid vehicle) [137] powertrain architectures. All the analyzed electric vehicles were optimized under the same driving cycle combination and the same optimization criteria applied in the current study. The only significant change is regarding the 3rd optimization criteria of the single HESS EV [63] that is related to EV acceleration performance instead of battery SoH.

For such evaluation, it was considered the lithium-ion battery price ratio of US$ 165/kWh, as reported by [143,144]. Concerning the electric motor, the costs were estimated based on the market database developed in an earlier study [94]. Lastly, the ultracapacitor costs can be evaluated by the ratio of US$ 66640/kWh (stored energy), as reported by [145].

Based on the provided results, it is possible to conclude that the best trade-off (max Ft) Dual HESS EV presents a cost-to-autonomy ratio enhancement of 44.42% and 49.97%, compared to the single HESS EV and EHHV configurations from previous studies, respectively. Although the optimal dual HESS-based EV configuration indeed presents a more expensive total cost of ownership when compared to the single HESS from this study, the extended driving autonomy of the dual HESS EV along with its benefits regarding long-term operating costs (an increase of battery lifetime) make such configuration more attractive than the single HESS-based one. The advantages of the dual HESS-equipped EV pay off the slight increase of the cost-to-range ratio (42.60 against 40.68) throughout vehicle operation. Therefore, the Dual HESS EV concept appears as a viable solution to popularize EVs in the automotive market

Table 9
Cost comparison between optimum Dual HESS EV, single HESS EV and EHHV.

Parameters	Dual HESS EV (current work)			
	max (f_1)	min (f_2)	max (f_3)	max (Ft)
Driving range [km]	369.16	98.34	223.98	285.56
Frontal battery cost	US$ 6673	US$ 1540	US$ 6294	US$ 5315
Frontal ultracapacitors cost	US$ 2339	US$ 1819	US$ 1819	US$ 1819
Frontal EMs cost	US$ 958	US$ 965	US$ 1124	US$ 1037
Rear battery cost	US$ 5964	US$ 706	US$ 2074	US$ 1871
Rear ultracapacitors cost	US$ 3358	US$ 1819	US$ 16 933	US$ 1819
Rear EMs cost	US$ 728	US$ 320	US$ 399	US$ 303
Powertrain overall cost	US$ 20 020	US$ 7169	US$ 28 643	US$ 12 164
$\frac{\text{Overall Cost}}{\text{Driving Range}}$ [US$/km]	54.23	72.90	127.88	42.60
	Single HESS EV (current work)			
	max (f_1)	min (f_2)	max (f_3)	max (Ft)
Driving range [km]	270.34	98.25	256.46	238.82
Battery cost	US$ 9019	US$ 2361	US$ 9140	US$ 6566
Ultracapacitor cost	US$ 1819	US$ 1819	US$ 1819	US$ 1819
Frontal EMs cost	US$ 1230	US$ 1120	US$ 1191	US$ 1136
Rear EMs cost	US$ 391	US$ 201	US$ 187	US$ 194
Powertrain overall cost	US$ 12 459	US$ 5501	US$ 12 337	US$ 9715
$\frac{\text{Overall Cost}}{\text{Driving Range}}$ [US$/km]	46.09	55.99	48.10	40.68
	Single HESS EV [63]			
	max (f_1)	min (f_2)	max (f_3)	max (Ft)
Driving range [km]	177.67	66.38	93.68	117.04
Battery cost	US$ 7629	US$ 2725	US$ 3735	US$ 4535
Ultracapacitor cost	US$ 5198	US$ 3145	US$ 12 835	US$ 3145
Frontal EMs cost	US$ 536	US$ 885	US$ 855	US$ 848
Rear EMs cost	US$ 385	US$ 530	US$ 625	US$ 444
Powertrain overall cost	US$ 13 748	US$ 7285	US$ 18 050	US$ 8972
$\frac{\text{Overall Cost}}{\text{Driving Range}}$ [US$/km]	77.38	109.75	192.67	76.66
	EHHV [137]			
	max (f_1)	min (f_2)	max (f_3)	max (Ft)
Driving range [km]	199.73	104.04	148.51	167.95
Battery cost	US$ 9508	US$ 4828	US$ 7012	US$ 7925
EM cost	US$ 4279	US$ 4273	US$ 4287	US$ 4300
Hydraulic drivetrain cost	US$ 2076	US$ 2076	US$ 2076	US$ 2076
Powertrain overall cost	US$ 15 863	US$ 11 177	US$ 13 375	US$ 14 301
$\frac{\text{Overall Cost}}{\text{Driving Range}}$ [US$/km]	79.42	107.43	90.06	85.15

5.3. Simulation under alternative driving cycles

In addition to the advantages mentioned above of the optimized solutions for Dual HESS-based EVs, it is also important to evaluate those configurations under driving profiles that are different from those in which the optimization method was conducted. In this sense, the optimum solutions were subjected to real-world urban driving cycles (Campinas [94], Ouro Branco [86] and Santa Maria [146,147] cycles), a real-world highway cycle (Campinas-to-São Paulo [125]) as well as the standard WLTC cycle.

As presented in Table 10, it is possible to infer that the optimized configurations achieved extended driving ranges, which were greater than 94 km (the minimum allowable autonomy set by the optimization constraints Eq. (49)), except to min f_2 solution under Campinas-to-São Paulo cycle. This is because the mentioned real-world driving cycle features a highway profile, which demands more power from the HESSs when compared to urban scenarios from Ouro Branco and Santa Maria cycles. Additionally, the EV configurations regenerate less in highway driving cycles, in which a limited number of stops and abrupt

Table 10
Optimized results under alternative driving cycles.

Results	Dual HESS EV solutions			
	Maximum driving range $\max(f_1)$	Minimum HESS mass $\min(f_2)$	Longest life cycle $\max(f_3)$	Best trade-off $\max(Ft)$
Campinas driving cycle [94]				
Driving range [km]	280.05	111.78	239.72	279.69
SoH_F	0.9978	0.9913	0.9977	0.9964
SoH_R	0.9973	0.9883	0.9941	0.9943
Front battery cycles ($SoH = 0.8$)	9868	9608	11 179	9667
Rear battery cycles ($SoH = 0.8$)	9692	6573	6196	5933
Ouro Branco driving cycle [86]				
Driving range [km]	460.05	112.72	243.94	312.09
SoH_F	0.9935	0.9807	0.9946	0.9915
SoH_R	0.9918	0.9729	0.9835	0.9857
Front battery cycles ($SoH = 0.8$)	5951	7525	13 854	6737
Rear battery cycles ($SoH = 0.8$)	4445	4423	4556	3932
Santa Maria driving cycle [146,147]				
Driving range [km]	361.37	124.72	242.84	305.43
SoH_F	0.997	0.9894	0.9975	0.9965
SoH_R	0.9957	0.9857	0.9928	0.9928
Front battery cycles ($SoH = 0.8$)	9757	8945	14 608	11 446
Rear battery cycles ($SoH = 0.8$)	9112	5997	6510	5285
Campinas to São Paulo driving cycle [125]				
Driving range [km]	350.93	57.66	168.59	239.04
SoH_F	0.9873	0.9811	0.9861	0.9852
SoH_R	0.9893	0.9761	0.9976	0.9879
Front battery cycles ($SoH = 0.8$)	5929	8411	9511	5211
Rear battery cycles ($SoH = 0.8$)	6783	15 182	10 639	9753
WLTC driving cycle				
Driving range [km]	389.19	103.23	239.54	292.27
SoH_F	0.9927	0.9742	0.9918	0.9899
SoH_R	0.9925	0.978	0.9926	0.9897
Front battery cycles ($SoH = 0.8$)	6425	4586	8169	5260
Rear battery cycles ($SoH = 0.8$)	6065	6296	11 955	6508

decelerations occur, thereby affecting the energy harvesting through regenerative braking.

In the WLTC cycle that combines low and high-speed routes, the optimal solutions presented a good performance for the batterie's life cycles. The same characteristic could be observed in the remaining driving conditions, in which the Campinas-to-São Paulo cycle showed the most reduced battery life expectation. As previously highlighted, this can be explained by its highway driving profile, which can eventually require higher power demand from the batteries.

6. Conclusion

In this work, a multi-objective optimization design of a dual HESS-based EV powertrain topology was developed to search for the best design variables concerning the maximum driving range and battery lifespan, and minimum system size. Moreover, the formulation of the optimization problem also considered the parameters of the fuzzy logic controllers that define the power management control for the proposed EV.

The proposed configuration aims to minimize battery discharge peaks by splitting the vehicle traction power demand between two independent traction systems, each one powered by its respective HESS system, allowing the use of alternative traction systems configuration and different arrangements of the batteries and ultracapacitors in each HESS. The results of this paper justify the importance of using hybrid energy storage systems in conjunction with the employment of a battery-aging-aware EMS, so that earlier battery end of life can be avoided by preventing such systems from being overloaded in high C-rate operational conditions (peak power demand).

The optimized dual HESS EV configuration reached a driving range up to 369.16 km, with a 566 kg energy storage system. On the other hand, the minimum mass solution got a 948.34 km driving range with a small energy storage pack of only 133 kg. Regarding the battery life cycle, the most promising solution reached up to 54 133 h and 65 562 h for the frontal and rear batteries, respectively. However, all these mentioned solutions only focused on providing the best result in a single optimization criterion, presenting drawbacks in the other ones. Therefore, the best dual HESS EV configuration was the one that showed the best trade-off among the three analyzed criteria, being able to reach a 285.56-km range with a 332-kg energy storage system, which endures for 36 585 h (frontal battery) and 38 201 h (rear battery).

The main contribution of this paper is to highlight the potential advantages of the proposed EV architecture when compared to the single HESS EV optimized under the same driving conditions. In this comparative analysis, the dual HESS presents a driving range per cost ratio 4.72% higher than the best single HESS EV solution. On the other hand, the dual HESS presents an approximate improvement of 3% in driving range per mass ratio and increases the batteries' lifetime by 17.68% (frontal) and 22.88% (rear), as compared to the single HESS EV, which makes the dual HESS powertrain more attractive considering a long-term operation.

Finally, the optimized dual HESS EV configurations were also evaluated under different driving cycles (some of the real-world driving cycles) to ensure that they are robust to driving conditions different from those applied in the optimization procedure. In all situations, the dual HESS EV proves to present satisfactory results.

It is essential to highlight that the optimization methods applied in this paper focus on the early concept of the dual HESS EV. The optimum values for the design variables of critical components such as electric motors, inverters, transmission systems, batteries, ultracapacitors, and buck-boost converters must be fitted to available market components. Furthermore, both energy storage systems need to be arranged correctly in an EV platform to reach a feasible EV to be experimentally evaluated.

Although the optimized dual HESS EV has shown promising results, some extra analyses such as the dynamic effects of HESS weight distribution in the EV driveability and handling control should be evaluated in future work. Moreover, training an artificial neural network to control the power management can also bring potential improvements to the vehicle. Finally, the combination of a hydrogen fuel cell stack with the HESS would be worthy of investigation due to its high potentiality with regard to driving autonomy, energy efficiency and energy storage systems' lifetime.

CRediT authorship contribution statement

Samuel Filgueira da Silva: Conceptualization, Methodology, Software, Investigation, Formal analysis, Validation, Data curation, Writing – original draft, Writing – review & editing, Visualization. **Jony Javorski Eckert:** Conceptualization, Methodology, Software, Investigation, Formal analysis, Validation, Data curation, Writing – original draft, Writing – review & editing, Visualization. **Fernanda Cristina Corrêa:** Conceptualization, Methodology, Software, Writing – original draft, Writing – review & editing, Visualization. **Fabrício Leonardo Silva:** Conceptualization, Methodology, Software, Investigation, Formal analysis, Writing – original draft, Writing – review & editing, Visualization. **Ludmila C.A. Silva:** Resources, Writing – review & editing, Supervision, Funding acquisition, Project administration. **Franco Giuseppe Dedini:** Resources, Writing – review & editing, Supervision, Funding acquisition, Project administration.

Declaration of competing interest

The authors declare that they have no known competing financial interests or personal relationships that could have appeared to influence the work reported in this paper.

Data availability

No data was used for the research described in the article.

Acknowledgments

This work was conducted during scholarships supported by the University of Campinas (UNICAMP), Brazil and the Federal Technological University of Paraná (UTFPR-PG), Brazil.

References

[1] Rafaj P, Kiesewetter G, Gül T, Schöpp W, Cofala J, Klimont Z, Purohit P, Heyes C, Amann M, Borken-Kleefeld J, et al. Outlook for clean air in the context of sustainable development goals. Global Environ Change 2018;53:1–11. http://dx.doi.org/10.1016/j.gloenvcha.2018.08.008.

[2] Hill G, Heidrich O, Creutzig F, Blythe P. The role of electric vehicles in near-term mitigation pathways and achieving the UK's carbon budget. Appl Energy 2019;251:113111. http://dx.doi.org/10.1016/j.apenergy.2019.04.107.

[3] Linn J, McConnell V. Interactions between federal and state policies for reducing vehicle emissions. Energy Policy 2019;126:507–17. http://dx.doi.org/10.1016/j.enpol.2018.10.052.

[4] Dhar S, Pathak M, Shukla PR. Electric vehicles and India's low carbon passenger transport: a long-term co-benefits assessment. J Cleaner Prod 2017;146:139–48. http://dx.doi.org/10.1016/j.jclepro.2016.05.111, Bridging the Gaps for Accelerating Low Carbon Actions in Asia.

[5] Organisation for Economic Co-Operation and Development. Energy technology perspectives 2017: catalysing energy technology transformations. Technical report, International Energy Agency; 2017.

[6] Frey HC. Trends in onroad transportation energy and emissions. J Air Waste Manage Assoc 2018;68(6):514–63. http://dx.doi.org/10.1080/10962247.2018.1454357.

[7] Sun R, Chen Y, Dubey A, Pugliese P. Hybrid electric buses fuel consumption prediction based on real-world driving data. Transp Res D 2021;91:102637. http://dx.doi.org/10.1016/j.trd.2020.102637.

[8] Hao H, Geng Y, Sarkis J. Carbon footprint of global passenger cars: Scenarios through 2050. Energy 2016;101:121–31. http://dx.doi.org/10.1016/j.energy.2016.01.089.

[9] Corno M, Pozzato G. Active adaptive battery aging management for electric vehicles. IEEE Trans Veh Technol 2020;69(1):258–69. http://dx.doi.org/10.1109/TVT.2019.2940033.

[10] Eldeeb HH, Elsayed AT, Lashway CR, Mohammed O. Hybrid energy storage sizing and power splitting optimization for plug-in electric vehicles. IEEE Trans Ind Appl 2019;55(3):2252–62. http://dx.doi.org/10.1109/TIA.2019.2898839.

[11] Farhadi M, Mohammed O. Energy storage technologies for high-power applications. IEEE Trans Ind Appl 2015;52(3):1953–61. http://dx.doi.org/10.1109/TIA.2015.2511096.

[12] Abdul-Quadir Y, Laurila T, Karppinen J, Jalkanen K, Vuorilehto K, Skogström L, Paulasto-Kröckel M. Heat generation in high power prismatic li-ion battery cell with LiMnNiCoO2 cathode material. Int J Energy Res 2014;38(11):1424–37. http://dx.doi.org/10.1002/er.3156.

[13] Zhang S, Xiong R. HESS and its application in series hybrid electric vehicles. In: Modeling, dynamics and control of electrified vehicles. Elsevier; 2018, p. 77–119. http://dx.doi.org/10.1016/B978-0-12-812786-5.00003-3.

[14] Power split strategies for hybrid energy storage systems for vehicular applications. J Power Sources 2014;258:395–407. http://dx.doi.org/10.1016/j.jpowsour.2014.01.118.

[15] Yu H, Dezza FC, Cheli F, Tang X, Hu X, Lin X. Dimensioning and power management of hybrid energy storage systems for electric vehicles with multiple optimization criteria. IEEE Trans Power Electron 2020. http://dx.doi.org/10.1109/TPEL.2020.3030822.

[16] Zhang S, Xiong R, Zhou X. Comparison of the topologies for a hybrid energy-storage system of electric vehicles via a novel optimization method. Sci China Technol Sci 2015;58(7):1173–85. http://dx.doi.org/10.1007/s11431-015-5843-y.

[17] Song Z, Hofmann H, Li J, Han X, Zhang X, Ouyang M. A comparison study of different semi-active hybrid energy storage system topologies for electric vehicles. J Power Sources 2015;274:400–11. http://dx.doi.org/10.1016/j.jpowsour.2014.10.061.

[18] Wang B, Xu J, Cao B, Zhou X. A novel multimode hybrid energy storage system and its energy management strategy for electric vehicles. J Power Sources 2015;281:432–43. http://dx.doi.org/10.1016/j.jpowsour.2015.02.012.

[19] Jung H, Wang H, Hu T. Control design for robust tracking and smooth transition in power systems with battery/supercapacitor hybrid energy storage devices. J Power Sources 2014;267:566–75. http://dx.doi.org/10.1016/j.jpowsour.2014.05.061.

[20] Sidharthan Panaparambil V, Kashyap Y, Vijay Castelino R. A review on hybrid source energy management strategies for electric vehicle. Int J Energy Res 2021;1–32. http://dx.doi.org/10.1002/er.7107.

[21] Shaker Y, Yousri D, Osama A, Al-Gindy A, Tag-Eldin E, Allam D. Optimal charging/discharging decision of energy storage community in grid-connected microgrid using multi-objective hunger game search optimizer. IEEE Access 2021;1. http://dx.doi.org/10.1109/ACCESS.2021.3101839.

[22] Herrera V, Milo A, Gaztañaga H, Etxeberria-Otadui I, Villarreal I, Camblong H. Adaptive energy management strategy and optimal sizing applied on a battery-supercapacitor based tramway. Appl Energy 2016;169:831–45. http://dx.doi.org/10.1016/j.apenergy.2016.02.079.

[23] Castaings A, Lhomme W, Trigui R, Bouscayrol A. Comparison of energy management strategies of a battery/supercapacitors system for electric vehicle under real-time constraints. Appl Energy 2016;163:190–200. http://dx.doi.org/10.1016/j.apenergy.2015.11.020.

[24] Yang B, Wang J, Zhang X, Wang J, Shu H, Li S, He T, Lan C, Yu T. Applications of battery/supercapacitor hybrid energy storage systems for electric vehicles using perturbation observer based robust control. J Power Sources 2020;448:227444. http://dx.doi.org/10.1016/j.jpowsour.2019.227444.

[25] Zhang S, Xiong R, Sun F. Model predictive control for power management in a plug-in hybrid electric vehicle with a hybrid energy storage system. Appl Energy 2017;185:1654–62. http://dx.doi.org/10.1016/j.apenergy.2015.12.035.

[26] Araujo RE, de Castro R, Pinto C, Melo P, Freitas D. Combined sizing and energy management in EVs with batteries and supercapacitors. IEEE Trans Veh Technol 2014;63(7):3062–76. http://dx.doi.org/10.1109/TVT.2014.2318275.

[27] Xiong R, Cao J, Yu Q. Reinforcement learning-based real-time power management for hybrid energy storage system in the plug-in hybrid electric vehicle. Appl Energy 2018;211:538–48. http://dx.doi.org/10.1016/j.apenergy.2017.11.072.

[28] Ibrahim M, Jemei S, Wimmer G, Hissel D. Nonlinear autoregressive neural network in an energy management strategy for battery/ultra-capacitor hybrid electrical vehicles. Electr Power Syst Res 2016;136:262–9. http://dx.doi.org/10.1016/j.epsr.2016.03.005.

[29] Masih-Tehrani M, Yazdi MRH, Esfahanian V, Dahmardeh M, Nehzati H. Wavelet-based power management for hybrid energy storage system. J Mod Power Syst Clean Energy 2019;7(4):779–90. http://dx.doi.org/10.1007/s40565-019-0529-2.

[30] Peng J, Wang R, Liao H, Zhou Y, Li H, Wu Y, Huang Z. A real-time layer-adaptive wavelet transform energy distribution strategy in a hybrid energy storage system of evs. Energies 2019;12(3):440. http://dx.doi.org/10.3390/en12030440.

[31] Song Z, Hofmann H, Li J, Hou J, Han X, Ouyang M. Energy management strategies comparison for electric vehicles with hybrid energy storage system. Appl Energy 2014;134:321–31. http://dx.doi.org/10.1016/j.apenergy.2014.08.035.

[32] Eckert JJ, d. A. Silva LC, Dedini FG, Corrêa FC. Electric vehicle powertrain and fuzzy control multi-objective optimization, considering dual hybrid energy storage systems. IEEE Trans Veh Technol 2020;69(4):3773–82. http://dx.doi.org/10.1109/TVT.2020.2973601.

[33] Silva LCA, Eckert JJ, Lourenço MAM, Silva FL, Corrêa FC, Dedini FG. Electric vehicle battery-ultracapacitor hybrid energy storage system and drivetrain optimization for a real-world urban driving scenario. J Braz Soc Mech Sci Eng 2021. http://dx.doi.org/10.1007/s40430-021-02975-w.

[34] Song Z, Li J, Han X, Xu L, Lu L, Ouyang M, Hofmann H. Multi-objective optimization of a semi-active battery/supercapacitor energy storage system for electric vehicles. Appl Energy 2014;135:212–24. http://dx.doi.org/10.1016/j.apenergy.2014.06.087.

[35] Song Z, Hofmann H, Li J, Han X, Ouyang M. Optimization for a hybrid energy storage system in electric vehicles using dynamic programing approach. Appl Energy 2015;139:151–62. http://dx.doi.org/10.1016/j.apenergy.2014.11.020.

[36] Li M, Wang L, Wang Y, Chen Z. Sizing optimization and energy management strategy for hybrid energy storage system using multiobjective optimization and random forests. IEEE Trans Power Electron 2021;36(10):11421–30. http://dx.doi.org/10.1109/TPEL.2021.3070393.

[37] Song Z, Zhang X, Li J, Hofmann H, Ouyang M, Du J. Component sizing optimization of plug-in hybrid electric vehicles with the hybrid energy storage system. Energy 2018;144:393–403. http://dx.doi.org/10.1016/j.energy.2017.12.009.

[38] Zhang S, Xiong R, Cao J. Battery durability and longevity based power management for plug-in hybrid electric vehicle with hybrid energy storage system. Appl Energy 2016;179:316–28. http://dx.doi.org/10.1016/j.apenergy.2016.06.153.

[39] Wieczorek M, Lewandowski M. A mathematical representation of an energy management strategy for hybrid energy storage system in electric vehicle and real time optimization using a genetic algorithm. Appl Energy 2017;192:222–33. http://dx.doi.org/10.1016/j.apenergy.2017.02.022.

[40] Hu X, Johannesson L, Murgovski N, Egardt B. Longevity-conscious dimensioning and power management of the hybrid energy storage system in a fuel cell hybrid electric bus. Appl Energy 2015;137:913–24. http://dx.doi.org/10.1016/j.apenergy.2014.05.013.

[41] Li S, Gu C, Zhao P, Cheng S. Adaptive energy management for hybrid power system considering fuel economy and battery longevity. Energy Convers Manage 2021;235:114004. http://dx.doi.org/10.1016/j.enconman.2021.114004.

[42] Sarvaiya S, Ganesh S, Xu B. Comparative analysis of hybrid vehicle energy management strategies with optimization of fuel economy and battery life. Energy 2021;228:120604. http://dx.doi.org/10.1016/j.energy.2021.120604.

[43] Nguyen B, Vo-Duy T, Henggeler Antunes C, Trovão JPF. Multi-objective benchmark for energy management of dual-source electric vehicles: An optimal control approach. Energy 2021;223:119857. http://dx.doi.org/10.1016/j.energy.2021.119857.

[44] Ostadi A, Kazerani M. A comparative analysis of optimal sizing of battery-only, ultracapacitor-only, and battery–ultracapacitor hybrid energy storage systems for a city bus. IEEE Trans Veh Technol 2015;64(10):4449–60. http://dx.doi.org/10.1109/TVT.2014.2371912.

[45] Mamun A-A, Liu Z, Rizzo DM, Onori S. An integrated design and control optimization framework for hybrid military vehicle using lithium-ion battery and supercapacitor as energy storage devices. IEEE Trans Transp Electrif 2019;5(1):239–51. http://dx.doi.org/10.1109/TTE.2018.2869038.

[46] Zhang L, Hu X, Wang Z, Sun F, Deng J, Dorrell DG. Multiobjective optimal sizing of hybrid energy storage system for electric vehicles. IEEE Trans Veh Technol 2017;67(2):1027–35. http://dx.doi.org/10.1109/TVT.2017.2762368.

[47] Li S, He H, Su C, Zhao P. Data driven battery modeling and management method with aging phenomenon considered. Appl Energy 2020;275:115340. http://dx.doi.org/10.1016/j.apenergy.2020.115340.

[48] Tang X, Zou C, Yao K, Lu J, Xia Y, Gao F. Aging trajectory prediction for lithium-ion batteries via model migration and Bayesian Monte Carlo method. Appl Energy 2019;254:113591. http://dx.doi.org/10.1016/j.apenergy.2019.113591.

[49] Severson KA, Attia PM, Jin N, Perkins N, Jiang B, Yang Z, Chen MH, Aykol M, Herring PK, Fraggedakis D, et al. Data-driven prediction of battery cycle life before capacity degradation. Nature Energy 2019;4(5):383–91.

[50] Hsu C-W, Xiong R, Chen N-Y, Li J, Tsou N-T. Deep neural network battery life and voltage prediction by using data of one cycle only. Appl Energy 2022;306:118134. http://dx.doi.org/10.1016/j.apenergy.2021.118134.

[51] Hu X, Yuan H, Zou C, Li Z, Zhang L. Co-estimation of state of charge and state of health for lithium-ion batteries based on fractional-order calculus. IEEE Trans Veh Technol 2018;67(11):10319–29. http://dx.doi.org/10.1109/TVT.2018.2865664.

[52] Li H, Ravey A, N'Diaye A, Djerdir A. Online adaptive equivalent consumption minimization strategy for fuel cell hybrid electric vehicle considering power sources degradation. Energy Convers Manage 2019;192:133–49. http://dx.doi.org/10.1016/j.enconman.2019.03.090.

[53] Mallon K, Assadian F. A study of control methodologies for the trade-off between battery aging and energy consumption on electric vehicles with hybrid energy storage systems. Energies 2022;15(2). http://dx.doi.org/10.3390/en15020600.

[54] Zhou Y, Cao S, Hensen JL. An energy paradigm transition framework from negative towards positive district energy sharing networks—Battery cycling aging, advanced battery management strategies, flexible vehicles-to-buildings interactions, uncertainty and sensitivity analysis. Appl Energy 2021;288:116606. http://dx.doi.org/10.1016/j.apenergy.2021.116606.

[55] Anselma PG, Kollmeyer P, Lempert J, Zhao Z, Belingardi G, Emadi A. Battery state-of-health sensitive energy management of hybrid electric vehicles: Lifetime prediction and ageing experimental validation. Appl Energy 2021;285:116440. http://dx.doi.org/10.1016/j.apenergy.2021.116440.

[56] De Pascali L, Biral F, Onori S. Aging-aware optimal energy management control for a parallel hybrid vehicle based on electrochemical-degradation dynamics. IEEE Trans Veh Technol 2020;69(10):10868–78. http://dx.doi.org/10.1109/TVT.2020.3019241.

[57] Yuksel T, Litster S, Viswanathan V, Michalek JJ. Plug-in hybrid electric vehicle LiFePO4 battery life implications of thermal management, driving conditions, and regional climate. J Power Sources 2017;338:49–64. http://dx.doi.org/10.1016/j.jpowsour.2016.10.104.

[58] Wang Z, Song C, Zhang L, Zhao Y, Liu P, Dorrell DG. A data-driven method for battery charging capacity abnormality diagnosis in electric vehicle applications. IEEE Trans Transp Electrif 2022;8(1):990–9. http://dx.doi.org/10.1109/TTE.2021.3117841.

[59] Hu J, Niu X, Jiang X, Zu G. Energy management strategy based on driving pattern recognition for a dual-motor battery electric vehicle. Int J Energy Res 2019;43(8):3346–64. http://dx.doi.org/10.1002/er.4474.

[60] Li Y, Huang X, Liu D, Wang M, Xu J. Hybrid energy storage system and energy distribution strategy for four-wheel independent-drive electric vehicles. J Cleaner Prod 2019;220:756–70. http://dx.doi.org/10.1016/j.jclepro.2019.01.257.

[61] Eckert JJ, Silva LC, Costa ES, Santiciolli FM, Dedini FG, Corrêa FC. Electric vehicle drivetrain optimisation. IET Electr Syst Transp 2017;7(1):32–40. http://dx.doi.org/10.1049/iet-est.2016.0022.

[62] Suh NP. Axiomatic design: advances and applications. USA: Oxford University Press; 2001.

[63] Eckert JJ, Silva LCdAe, Santiciolli FM, Costa EdS, Corrêa FC, Dedini FG. Energy storage and control optimization for an electric vehicle. Int J Energy Res 2018;42(11):3506–23. http://dx.doi.org/10.1002/er.4089.

[64] Hochgraf CG, Basco JK, Bohn TP, Bloom I. Effect of ultracapacitor-modified PHEV protocol on performance degradation in lithium-ion cells. J Power Sources 2014;246:965–9. http://dx.doi.org/10.1016/j.jpowsour.2012.09.038.

[65] Vora AP, Jin X, Hoshing V, Shaver G, Varigonda S, Tyner WE. Integrating battery degradation in a cost of ownership framework for hybrid electric vehicle design optimization. Proc Inst Mech Eng D 2019;233(6):1507–23. http://dx.doi.org/10.1177/0954407018802663.

[66] Sakti A, Michalek JJ, Fuchs ER, Whitacre JF. A techno-economic analysis and optimization of Li-ion batteries for light-duty passenger vehicle electrification. J Power Sources 2015;273:966–80. http://dx.doi.org/10.1016/j.jpowsour.2014.09.078.

[67] Baghdadi I, Briat O, Delétage J-Y, Gyan P, Vinassa J-M. Lithium battery aging model based on dakin's degradation approach. J Power Sources 2016;325:273–85. http://dx.doi.org/10.1016/j.jpowsour.2016.06.036.

[68] Xie S, Qi S, Lang K, Tang X, Lin X. Coordinated management of connected plug-in hybrid electric buses for energy saving, inter-vehicle safety, and battery health. Appl Energy 2020;268:115028. http://dx.doi.org/10.1016/j.apenergy.2020.115028.

[69] Bai Y, He H, Li J, Li S, xiong Wang Y, Yang Q. Battery anti-aging control for a plug-in hybrid electric vehicle with a hierarchical optimization energy management strategy. J Cleaner Prod 2019;237:117841. http://dx.doi.org/10.1016/j.jclepro.2019.117841.

[70] Uddin K, Moore AD, Barai A, Marco J. The effects of high frequency current ripple on electric vehicle battery performance. Appl Energy 2016;178:142–54. http://dx.doi.org/10.1016/j.apenergy.2016.06.033.

[71] Woody M, Arbabzadeh M, Lewis GM, Keoleian GA, Stefanopoulou A. Strategies to limit degradation and maximize Li-ion battery service lifetime - critical review and guidance for stakeholders. J Energy Storage 2020;28:101231. http://dx.doi.org/10.1016/j.est.2020.101231.

[72] Jing R, Wang J, Shah N, Guo M. Emerging supply chain of utilising electrical vehicle retired batteries in distributed energy systems. Adv Appl Energy 2021;1:100002. http://dx.doi.org/10.1016/j.adapen.2020.100002.

[73] Fallah N, Fitzpatrick C, Killian S, Johnson M. End-of-life electric vehicle battery stock estimation in Ireland through integrated energy and circular economy modelling. Resour Conserv Recy 2021;174:105753. http://dx.doi.org/10.1016/j.resconrec.2021.105753.

[74] Guo M, Mu Y, Jia H, Deng Y, Xu X, Yu X. Electric/thermal hybrid energy storage planning for park-level integrated energy systems with second-life battery utilization. Adv Appl Energy 2021;4:100064. http://dx.doi.org/10.1016/j.adapen.2021.100064.

[75] Peterson SB, Michalek JJ. Cost-effectiveness of plug-in hybrid electric vehicle battery capacity and charging infrastructure investment for reducing US gasoline consumption. Energy Policy 2013;52:429–38. http://dx.doi.org/10.1016/j.enpol.2012.09.059, Special Section: Transition Pathways to a Low Carbon Economy.

[76] Li Y, Xie K, Wang L, Xiang Y. The impact of PHEVs charging and network topology optimization on bulk power system reliability. Electr Power Syst Res 2018;163:85–97. http://dx.doi.org/10.1016/j.epsr.2018.06.002.

[77] Gilleran M, Bonnema E, Woods J, Mishra P, Doebber I, Hunter C, Mitchell M, Mann M. Impact of electric vehicle charging on the power demand of retail buildings. Adv Appl Energy 2021;4:100062. http://dx.doi.org/10.1016/j.adapen.2021.100062.

[78] Li H, Wang Z, Hong T, Piette MA. Energy flexibility of residential buildings: A systematic review of characterization and quantification methods and applications. Adv Appl Energy 2021;3:100054. http://dx.doi.org/10.1016/j.adapen.2021.100054.

[79] Hu X, Martinez CM, Yang Y. Charging, power management, and battery degradation mitigation in plug-in hybrid electric vehicles: A unified cost-optimal approach. Mech Syst Signal Process 2017;87:4–16. http://dx.doi.org/10.1016/j.ymssp.2016.03.004, Signal Processing and Control challenges for Smart Vehicles.

[80] Zhang H, Chen J, Yan J, Song X, Shibasaki R, Yan J. Urban power load profiles under ageing transition integrated with future EVs charging. Adv Appl Energy 2021;1:100007. http://dx.doi.org/10.1016/j.adapen.2020.100007.

[81] Woo S, Bae S, Moura SJ. Pareto optimality in cost and service quality for an electric vehicle charging facility. Appl Energy 2021;290:116779. http://dx.doi.org/10.1016/j.apenergy.2021.116779.

[82] Englberger S, Chapman AC, Tushar W, Almomani T, Snow S, Witzmann R, Jossen A, Hesse H. Evaluating the interdependency between peer-to-peer networks and energy storages: A techno-economic proof for prosumers. Adv Appl Energy 2021;3:100059. http://dx.doi.org/10.1016/j.adapen.2021.100059.

[83] Woo J, Choi H, Ahn J. Well-to-wheel analysis of greenhouse gas emissions for electric vehicles based on electricity generation mix: A global perspective. Transp Res D 2017;51:340–50. http://dx.doi.org/10.1016/j.trd.2017.01.005.

[84] Davies J, Kurani KS. Moving from assumption to observation: Implications for energy and emissions impacts of plug-in hybrid electric vehicles. Energy Policy 2013;62:550–60. http://dx.doi.org/10.1016/j.enpol.2013.06.126.

[85] Gillespie TD. Fundamentals of vehicle dynamics. Society of Automotive Engineers - SAE; 1992.

[86] Barbosa TP, Eckert JJ, Silva LCA, da Silva LAR, Gutiérrez JCH, Dedini FG. Gear shifting optimization applied to a flex-fuel vehicle under real driving conditions. Mech Based Des Struct Mach 2022;50(6):2084–101. http://dx.doi.org/10.1080/15397734.2020.1769650.

[87] Barlow TJ, Latham S, McCrae I, Boulter P. A reference book of driving cycles for use in the measurement of road vehicle emissions. TRL published project report, 2009.

[88] Giakoumis EG. Driving and engine cycles, Vol. 1. Springer; 2017, p. XX–408. http://dx.doi.org/10.1007/978-3-319-49034-2.

[89] Eckert JJ, Santiciolli FM, Silva LCA, Dedini FG. Vehicle drivetrain design multi-objective optimization. Mech Mach Theory 2021;156(1). http://dx.doi.org/10.1016/j.mechmachtheory.2020.104123.

[90] Eckert J, Santiciolli F, Yamashita R, Correa F, Silva LC, Dedini F. Fuzzy gear shifting control optimization to improve vehicle performance, fuel consumption and engine emissions. IET Control Theory Appl 2019. http://dx.doi.org/10.1049/iet-cta.2018.6272.

[91] Jazar RN. Vehicle dynamics. Springer; 2008.

[92] Tong W. Mechanical design of electric motors. CRC Press; 2014.

[93] Yamashita RY, Silva FL, Santiciolli FM, Eckert JJ, Dedini FG, Silva LC. Comparison between two models of BLDC motor, simulation and data acquisition. J Braz Soc Mech Sci Eng 2018;40(2):1–11. http://dx.doi.org/10.1007/s40430-018-1020-0.

[94] Eckert JJ, da Silva SF, de Menezes Lourenço MA, Corrêa FC, Silva LC, Dedini FG. Energy management and gear shifting control for a hybridized vehicle to minimize gas emissions, energy consumption and battery aging. Energy Convers Manage 2021;240:114222. http://dx.doi.org/10.1016/j.enconman.2021.114222.

[95] da Silva SF, Eckert JJ, Silva FL, Silva LC, Dedini FG. Multi-objective optimization design and control of plug-in hybrid electric vehicle powertrain for minimization of energy consumption, exhaust emissions and battery degradation. Energy Convers Manage 2021;234:113909. http://dx.doi.org/10.1016/j.enconman.2021.113909.

[96] Rotering N, Ilic M. Optimal charge control of plug-in hybrid electric vehicles in deregulated electricity markets. IEEE Trans Power Syst 2010;26(3):1021–9. http://dx.doi.org/10.1109/TPWRS.2010.2086083.

[97] Choi M-E, Lee J-S, Seo S-W. Real-time optimization for power management systems of a battery/supercapacitor hybrid energy storage system in electric vehicles. IEEE Trans Veh Technol 2014;63(8):3600–11. http://dx.doi.org/10.1109/TVT.2014.2305593.

[98] Ehsani M, Gao Y, Longo S, Ebrahimi KM. Modern electric, hybrid electric, and fuel cell vehicles. CRC Press; 2018, http://dx.doi.org/10.1201/9780429504884.

[99] Cao J, Emadi A. A new battery/ultracapacitor hybrid energy storage system for electric, hybrid, and plug-in hybrid electric vehicles. IEEE Trans Power Electron 2011;27(1):122–32.

[100] Vazquez S, Lukic SM, Galvan E, Franquelo LG, Carrasco JM. Energy storage systems for transport and grid applications. IEEE Trans Ind Electron 2010;57(12):3881–95.

[101] Geetha A, Subramani C. A comprehensive review on energy management strategies of hybrid energy storage system for electric vehicles. Int J Energy Res 2017;41(13):1817–34.

[102] Seixas LD, Tosso HG, Corrêa FC, Eckert JJ. Particle swarm optimization of a fuzzy controlled hybrid energy storage system - HESS. In: 2020 IEEE vehicle power and propulsion conference (VPPC). 2020, p. 1–6. http://dx.doi.org/10.1109/VPPC49601.2020.9330939.

[103] Khaligh A, Li Z. Battery, ultracapacitor, fuel cell, and hybrid energy storage systems for electric, hybrid electric, fuel cell, and plug-in hybrid electric vehicles: State of the art. IEEE Trans Veh Technol 2010;59(6):2806–14.

[104] Li M, Xu H, Li W, Liu Y, Li F, Hu Y, Liu L. The structure and control method of hybrid power source for electric vehicle. Energy 2016;112:1273–85. http://dx.doi.org/10.1016/j.energy.2016.06.009.

[105] Moseley PT, Garche J. Electrochemical energy storage for renewable sources and grid balancing. Newnes; 2014, http://dx.doi.org/10.1016/C2012-0-01253-7.

[106] Thackeray MM, Wolverton C, Isaacs ED. Electrical energy storage for transportation—approaching the limits of, and going beyond, lithium-ion batteries. Energy Environ Sci 2012;5(7):7854–63. http://dx.doi.org/10.1039/C2EE21892E.

[107] Wang C-Y, Zhang G, Ge S, Xu T, Ji Y, Yang X-G, Leng Y. Lithium-ion battery structure that self-heats at low temperatures. Nature 2016;529(7587):515–8. http://dx.doi.org/10.1038/nature16502.

[108] Shepherd CM. Design of primary and secondary cells: II. An equation describing battery discharge. J Electrochem Soc 1965;112(7):657.

[109] Tremblay O, Dessaint L-A. Experimental validation of a battery dynamic model for ev applications. World Electr Veh J 2009;3(2):289–98.

[110] Saw L, Somasundaram K, Ye Y, Tay A. Electro-thermal analysis of lithium iron phosphate battery for electric vehicles. J Power Sources 2014;249:231–8. http://dx.doi.org/10.1016/j.jpowsour.2013.10.052.

[111] Delfino F, Ferro G, Minciardi R, Robba M, Rossi M, Rossi M. Identification and management of an electrical storage system for application in photovoltaic installations. In: 2017 13th IEEE international conference on control automation (ICCA). 2017, p. 886–91. http://dx.doi.org/10.1109/ICCA.2017.8003178.

[112] Delfino F, Ferro G, Minciardi R, Robba M, Rossi M, Rossi M. Identification and optimal control of an electrical storage system for microgrids with renewables. Sustain Energy Grids Netw 2019;17:100183. http://dx.doi.org/10.1016/j.segan.2018.100183.

[113] Young K, Wang C, Strunz K, et al. Electric vehicle battery technologies. In: Electric vehicle integration into modern power networks. Springer; 2013, p. 15–56.

[114] Motapon SN, Lachance E, Dessaint L-A, Al-Haddad K. A generic cycle life model for lithium-ion batteries based on fatigue theory and equivalent cycle counting. IEEE Open J Ind Electron Soc 2020;1:207–17. http://dx.doi.org/10.1109/OJIES.2020.3015396.

[115] Zhang L, Hu X, Wang Z, Sun F, Dorrell DG. A review of supercapacitor modeling, estimation, and applications: A control/management perspective. Renew Sustain Energy Rev 2018;81:1868–78. http://dx.doi.org/10.1016/j.rser.2017.05.283.

[116] Lu L, Han X, Li J, Hua J, Ouyang M. A review on the key issues for lithium-ion battery management in electric vehicles. J Power Sources 2013;226:272–88. http://dx.doi.org/10.1016/j.jpowsour.2012.10.060.

[117] Omar N, Monem MA, Firouz Y, Salminen J, Smekens J, Hegazy O, Gaulous H, Mulder G, Van den Bossche P, Coosemans T, Van Mierlo J. Lithium iron phosphate based battery – Assessment of the aging parameters and development of cycle life model. Appl Energy 2014;113:1575–85. http://dx.doi.org/10.1016/j.apenergy.2013.09.003.

[118] ISO, Electrically propelled road vehicles - Test specification for lithium-ion traction battery packs and systems - Part 2: High-energy applications (ISO Standard No.12405-2:2012) pp. 1–60.

[119] Shi D, Liu S, Cai Y, Wang S, Li H, Chen L. Pontryagin's minimum principle based fuzzy adaptive energy management for hybrid electric vehicle using real-time traffic information. Appl Energy 2021;286:116467. http://dx.doi.org/10.1016/j.apenergy.2021.116467.

[120] Li P, Jiao X, Li Y. Adaptive real-time energy management control strategy based on fuzzy inference system for plug-in hybrid electric vehicles. Control Eng Pract 2021;107:104703. http://dx.doi.org/10.1016/j.conengprac.2020.104703.

[121] Yang C, Liu K, Jiao X, Wang W, Chen R, You S. An adaptive firework algorithm optimization-based intelligent energy management strategy for plug-in hybrid electric vehicles. Energy 2021;122120. http://dx.doi.org/10.1016/j.energy.2021.122120.

[122] Rahman AU, Zehra SS, Ahmad I, Armghan H. Fuzzy supertwisting sliding mode-based energy management and control of hybrid energy storage system in electric vehicle considering fuel economy. J Energy Storage 2021;37:102468. http://dx.doi.org/10.1016/j.est.2021.102468.

[123] Wang S, Liu Y, Wang Z, Dong P, Cheng Y, Xu X, Tenberge P. Adaptive fuzzy iterative control strategy for the wet-clutch filling of automatic transmission. Mech Syst Signal Process 2019;130:164–82. http://dx.doi.org/10.1016/j.ymssp.2019.05.008.

[124] Silva FL, Silva LC, Eckert JJ, de Menezes Lourenço MA. Robust fuzzy stability control optimization by multi-objective for modular vehicle. Mech Mach Theory 2022;167:104554. http://dx.doi.org/10.1016/j.mechmachtheory.2021.104554.

[125] Miranda MH, Silva FL, Lourenço MA, Eckert JJ, Silva LC. Electric vehicle powertrain and fuzzy controller optimization using a planar dynamics simulation based on a real-world driving cycle. Energy 2021;121979. http://dx.doi.org/10.1016/j.energy.2021.121979.

[126] Silva FL, da Silva SF, Mazzariol FS, Eckert JJ, Silva LCA, Dedini FG. Multi-objective optimization of the steering system and fuzzy logic control applied to a car-like robot. In: Multibody mechatronic systems. Cham: Springer International Publishing; 2021, p. 195–202. http://dx.doi.org/10.1007/978-3-030-60372-4_22.

[127] Guenounou O, Dahhou B, Chabour F. Adaptive fuzzy controller based MPPT for photovoltaic systems. Energy Convers Manage 2014;78:843–50. http://dx.doi.org/10.1016/j.enconman.2013.07.093.

[128] Long S, Geng S. Decision framework of photovoltaic module selection under interval-valued intuitionistic fuzzy environment. Energy Convers Manage 2015;106:1242–50. http://dx.doi.org/10.1016/j.enconman.2015.10.037.

[129] Beddar A, Bouzekri H, Babes B, Afghoul H. Experimental enhancement of fuzzy fractional order PI+I controller of grid connected variable speed wind energy conversion system. Energy Convers Manage 2016;123:569–80. http://dx.doi.org/10.1016/j.enconman.2016.06.070.

[130] Mahmoudi SM, Maleki A, Rezaei Ochbelagh D. Optimization of a hybrid energy system with/without considering back-up system by a new technique based on fuzzy logic controller. Energy Convers Manage 2021;229:113723. http://dx.doi.org/10.1016/j.enconman.2020.113723.

[131] Li E-H, Li Y-Z, Xie J-Y, Sun Y-H, Yang L-Z, Ning X-W. A fuzzy coordination control of a water membrane evaporator cooling system for aerospace electronics. Appl Therm Eng 2021;191:116872. http://dx.doi.org/10.1016/j.applthermaleng.2021.116872.

[132] Dong S-J, Li Y-Z, Wang J, Wang J. Fuzzy incremental control algorithm of loop heat pipe cooling system for spacecraft applications. Comput Math Appl 2012;64(5):877–86. http://dx.doi.org/10.1016/j.camwa.2012.01.030, Advanced Technologies in Computer, Consumer and Control.

[133] Poursamad A, Montazeri M. Design of genetic-fuzzy control strategy for parallel hybrid electric vehicles. Control Eng Pract 2008;16(7):861–73.

[134] Çeven S, Albayrak A, Bayır R. Real-time range estimation in electric vehicles using fuzzy logic classifier. Comput Electr Eng 2020;83:106577. http://dx.doi.org/10.1016/j.compeleceng.2020.106577.

[135] Mahmoud M. Fuzzy control, estimation and diagnosis: Single and interconnected systems. 2018, http://dx.doi.org/10.1007/978-3-319-54954-5.
[136] Gen M, Cheng R, Lin L. Network models and optimization: multiobjective genetic algorithm approach. Springer Science & Business Media; 2008.
[137] Eckert JJ, Barbosa TP, da Silva SF, Silva FL, Silva LC, Dedini FG. Electric hydraulic hybrid vehicle powertrain design and optimization-based power distribution control to extend driving range and battery life cycle. Energy Convers Manage 2022;252:115094. http://dx.doi.org/10.1016/j.enconman.2021.115094.
[138] Barbosa TP, Eckert JJ, Roso VR, Pacheco Pujatti FJ, Rodrigues da Silva LA, Horta Gutiérrez JC. Fuel saving and lower pollutants emissions using an ethanol-fueled engine in a hydraulic hybrid passengers vehicle. Energy 2021;235:121361. http://dx.doi.org/10.1016/j.energy.2021.121361.
[139] Eckert JJ, Barbosa TP, Silva FL, Roso VR, Silva LC, da Silva LAR. Optimum fuzzy logic controller applied to a hybrid hydraulic vehicle to minimize fuel consumption and emissions. Expert Syst Appl 2022;207:117903. http://dx.doi.org/10.1016/j.eswa.2022.117903.
[140] Eckert JJ, da Silva SF, Santiciolli FM, de Carvalho AC, Dedini FG. Multi-speed gearbox design and shifting control optimization to minimize fuel consumption, exhaust emissions and drivetrain mechanical losses. Mech Mach Theory 2022;169:104644. http://dx.doi.org/10.1016/j.mechmachtheory.2021.104644.
[141] Lopes MV, Dias APC, Eckert JJ, Santos AA. Design of triple-beam internal-impact piezoelectric harvester optimized for energy and bandwidth. J Braz Soc Mech Sci Eng 2022;44(6):1–14. http://dx.doi.org/10.1007/s40430-022-03553-4.
[142] Lopes MV, Eckert JJ, Martins TS, dos Santos AA. Multi-objective optimization of piezoelectric vibrational energy harvester orthogonal spirals for ore freight cars. J Braz Soc Mech Sci Eng 2021;43(6):1–13. http://dx.doi.org/10.1007/s40430-021-03014-4.
[143] Berckmans G, Messagie M, Smekens J, Omar N, Vanhaverbeke L, Van Mierlo J. Cost projection of state of the art lithium-ion batteries for electric vehicles up to 2030. Energies 2017;10(9). http://dx.doi.org/10.3390/en10091314.
[144] Lutsey N, Nicholas M. Update on electric vehicle costs in the United States through 2030. In: The international council on clean transportation, Vol. 2. 2019.
[145] Mongird K, Viswanathan VV, Balducci PJ, Alam MJE, Fotedar V, Koritarov VS, Hadjerioua B. Energy storage technology and cost characterization report. Tech. rep., Richland, WA (United States): Pacific Northwest National Lab.(PNNL); 2019.
[146] Roso VR, Martins MES. Simulation of fuel consumption and emissions for passenger cars and urban buses in real-world driving cycles. Tech. rep., SAE Technical Paper; 2016, http://dx.doi.org/10.4271/2016-36-0443.
[147] Roso VR, Santos NDSA, Valle RM, Alvarez CEC, Monsalve-Serrano J, García A. Evaluation of a stratified prechamber ignition concept for vehicular applications in real world and standardized driving cycles. Appl Energy 2019;254:113691. http://dx.doi.org/10.1016/j.apenergy.2019.113691.